Studies on dielectric properties of sapphire between 10GHz-40GHz

by

Haotian Wang

Submitted in Partial Fulfillment of the

Requirements for the Degree

Master of Science

Supervised by

Professor Alexander Schmidt

Faculty of Mathematics, Computer Science and Natural Sciences
Department of Physics

Rheinisch-Westfälische Technische Hochschule Aachen
Aachen, Deutschland

November 7, 2022

Declaration

I declare that the work contained in this thesis is my own, except where explicitly stated otherwise. In addition this work has not been submitted to obtain another degree or professional qualification.

Signed:____

Date:____

Acknowledgments

I would like to show my gratitude to Professor Alexander Schmidt, who provided me with this opportunity to do research and this interesting topic to work on and gave me feedback on my progress. I am also quite grateful to Erdem Öz, who gave me instructions on doing experiment, proofread this thesis and gave many useful suggestions. In addition, he also helped me a lot in the cryogenic experiment and so did Tim Kuhlbusch, whom I would like to thank a lot as well. Finally, I would like to thank my parents Lida and Yanjing, who support and encourage me all the time at both happy and sad moments.

Table of Contents

Abstract

Sapphire is one of the main candidate materials to be used in the dielectric haloscope of the MADMAX(MAgnetized Disk and Mirror Axion eXperiment) project. The perpendicular component of its dielectric properties have been investigated in the frequency range 10-40 GHz at room temperature (295-297 K) and at 18 K in a dry cryostat using a microwave resonator. Detailed analysis of the measurements are reported and similar measurements and theoretical models from the literature are discussed. MADMAX is to search for the axion which is a cold dark matter candidate. In the haloscope, multiple dielectric disks are placed in a row parallel to each other to enhance the theorized microwave signal that is generated at the interfaces in the presence of a magnetic field. For the MADMAX project knowing the dielectric properties of the disk materials is crucial since it affects the enhancement factor.

1 Introduction

The axion is a new kind of hypothetical particle suggested by Peccei and Quinn[1]. It is a promising candidate for cold dark matter (DM[2]), which is the missing matter in the universe. In addition, it provides a possible solution to why there is an absence of strong charge-parity violating effects in quantum chromodynamics (QCD)[3]. It is such an important particle that a large number of experiments have been proposed or carried out trying to prove its existence, among which is MADMAX[4]. Theoretically, axions are bosons with a low mass smaller than 1 meV. In the scenario where the PQ symmetry breaking happened after inflation, a value of mass around 100 μeV is predicted.

1.1 Working principle of MADMAX

The possibility to detect axions is based on the predicted weak interaction of the axion with photons. This will add a new interaction term in the Lagrangian of the electromagnetic field[5]:

$$\mathcal{L}_{int} = -\frac{g_{a\gamma}}{4} F_{\mu\nu}\tilde{F}^{\mu\nu} a \tag{1.1}$$

Where $g_{a\gamma}$ is the coupling constant, $F_{\mu\nu}$ is the field strength for electromagnetic field, $\tilde{F}^{\mu\nu} = \frac{1}{2}\varepsilon^{\alpha\beta\mu\nu}F_{\alpha\beta}$ with $\varepsilon^{0123} = 1$, and a is the axion field. After applying the Euler-Lagrange equation to the whole Lagrangian, one gets the modified Maxwell's equations. In the presence of a strong homogeneous external magnetic field, the axion induced electric field is:

$$\mathbf{E}_a(t) = -\frac{g_{a\gamma\mathbf{B}_e}}{\epsilon} a(t) \tag{1.2}$$

Where $\mathbf{B}_e$ is the homogeneous external magnetic field. Existence of this field means that in the presence of a discontinuity of the permittivity of the medium, an electromagnetic field must be generated in order to satisfy the continuity of the fields. However, the

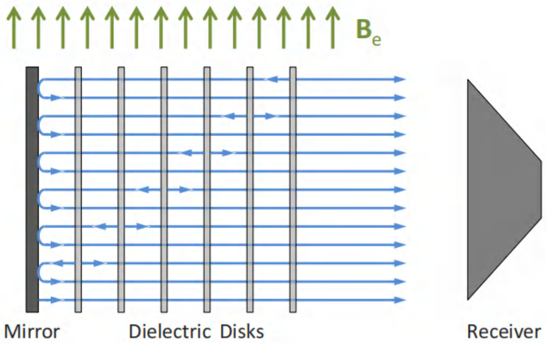

Figure 1.1: A sketch for the dielectric haloscope[5].

energy density of this induced electromagnetic field is so small that it is beyond the range that we can detect, so many methods have been proposed to solve this problem among which is a setup called dielectric haloscope.

Dielectric haloscopes are mainly composed of multiple disks made of dielectric materials. The disks are parallel to each other and arranged in a line parallel to the ground with the centres of all the surfaces of the disks on the line. A mirror is placed on one side in order to reflect back the electromagnetic signal and a receiver is put on the other side to receive the signal(figure 1.1). When we introduce a homogeneous external magnetic field parallel to surfaces of disks, according to (1.2), an electric field parallel to surfaces will be induced by the axion field. Axions are deemed to be non-relativistic particles on the Earth. The velocity is thought to be around 10^{-3} and the de Brogile wavelength is about 12.4 m, which means that we can consider the axion field to be a homogeneous field over scales smaller than this value. Consequently, for axions of a certain mass m_a, the axion field can be described in natural unit as:

$$a(t) = a_0 e^{im_a t} \tag{1.3}$$

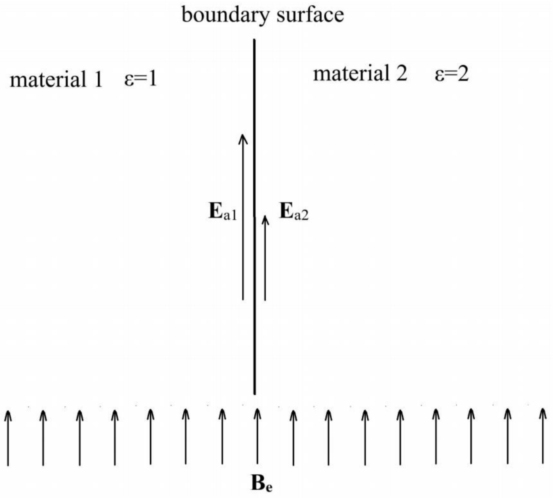

Figure 1.2: Discontinuity caused by difference in permittivity at the boundary

According to (1.2), if the external magnetic field and the axion field are fixed, the induced electric field is only dependent on the permittivity ϵ. As a result, if we put a boundary surface separating two regions of different ϵ, the axion-induced electric field will not be continuous any more at the boundary (See Figure 1.2). From the modified Maxwell's equations we know that the parallel components of **E** and **H** at the boundary must be continuous so there must be extra electromagnetic waves compensating for the discontinuity. These waves are radiated out from the boundary and propagate in the perpendicular direction out of the surface. Multiple dielectric layers in the haloscope create many different regions so that there are many waves emitted from, reflected or transmitted through these interfaces. By selecting thickness of the disks and adjusting the distance between them properly, these coherent waves can be amplified by constructive interference and resonance and be detectable.

To summarize, the ubiquitous axion field is expected to induce electromagnetic waves at the interface of two different media in a strong homogeneous magnetic field. Then the dielectric haloscope composed of many such interfaces amplifies these coherent waves by constructive interference among them and then the induced signal can be detected.

1.2 Why MADMAX needs dielectric properties of sapphire

There are two basic requirements for the dielectric disks in the haloscope. One is having high permittivity, in other words, high dielectric constant because the higher the dielectric constant is, the more noticeable the discontinuity is. The other is having low loss for electromagnetic waves since we do not want the wave to dissipate so much before it reaches the receiver. There are currently two candidate materials satisfying these demands. One is lanthanum aluminate (LaAlO_3) with a dielectric constant about 24 and loss tangent less than 10^{-6} at cryogenic temperatures. The other is sapphire ($\alpha - Al_2O_3$).

The frequency ν of the induced electromagnetic wave depends on the mass of axions:

$$\nu = \frac{m_a c^2}{h} \tag{1.4}$$

Where h is the Planck constant and c is the speed of light in vacuum. MADMAX focuses on the axion mass range 40-400 μeV corresponding to electromagnetic wave frequency range 9.7-97 GHz. Since the dielectric properties are temperature and frequency dependent, here we concentrate on the range 10-40 GHz. The boost factor of the dielectric haloscope is affected by the dielectric properties of the disk material. For example, in the work by Knirck[6], the ratio of boost factor with a loss angle δ to that without loss is given by

$$\frac{\beta_\delta^2}{\beta_0^2} = \frac{1}{4N^2}\left|\frac{1 - exp[-N\delta|n|\omega d]}{1 - exp[-\frac{\delta}{2}|n|\omega d]}\right|^2 \tag{1.5}$$

Where β_δ and β_0 are boost factors with and without loss, N is the number of layers in the dielectric haloscope, d is the thickness of each layer and n is the refractive index of the disk material. In addition, figure 1.3 shows the relation between the reduction of the power boost factor and $tan\delta$. Thus, it is crucial to know the dielectric loss which has an effect on the boost factor when designing the dielectric haloscope.

A number of experiments exist in literature reporting dielectric constant and loss tangent of sapphire at different frequencies and temperatures. The principal experimental method is to use a cylinder microwave resonator with a cylinder sapphire sample in it. The sapphire crystals are mostly cut so that the c axis is parallel to the cylinder axis to make sure the whole set up is cylindrically symmetric. Then a function

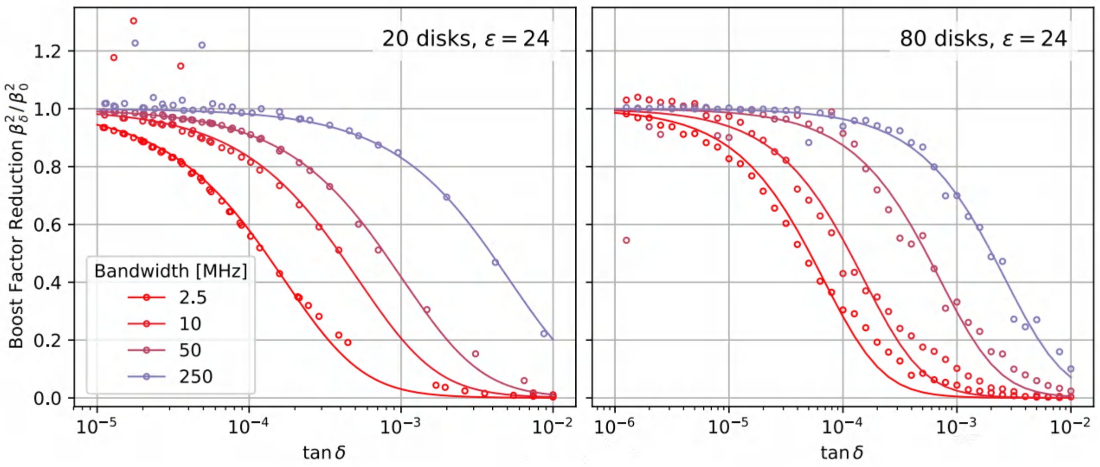

Figure 1.3: Relations between the reduction of the power boost factor and $tan\delta$ for 20 disks at ∼ 18 GHz (left) and 80 disks at ∼ 22 GHz (right)[6]

between resonance frequency and dielectric constant can be established by applying the radial mode matching method to the system[7, 8]. Resonance frequencies of the system can be measured and used to calculate the dielectric constant. For loss tangent, a formula can be also derived and some parameters in the formula need to be calculated in a simulation software. These are discussed in details in the following chapter. Hartnett, Tobar and Krupka[9] reported that parallel component of loss tangent of sapphire $tan\delta_{||} = (4.2 \pm 1.0) \times 10^{-7} f^{(1.09 \pm 0.09)}$ and perpendicular component $tan\delta_{\perp} = (1.3 \pm 0.2) \times 10^{-6} f^{(0.84 \pm 0.05)}$ where f is resonance frequency in GHz, at 296 K and in the frequency range 7-16 GHz. In another work by Krupka[10], perpendicular component of dielectric constant, $\epsilon_\perp$, is measured to be 9.27 at 15 K and 9.4 at 298 K at 21 GHz and parallel component one $\epsilon_{||}$ to be 11.34 and 11.59 respectively. $tan\delta_\perp$ and $tan\delta_{||}$ are reported to be around 10^{-8} at 19 K and 10^{-5} at 298 K respectively.

In this thesis, the perpendicular components of sapphire dielectric properties have been studied at room temperatures, 295-297 K, and at 18 K. The thesis is structured as follows: In chapter 2, the concepts of the dielectric constant and loss tangent are reviewed and formulas needed for the measurement are presented. In chapter 3, detailed procedures of the experiment are reported. Results of those experiments are presented in chapter 4 and data from other literature are also cited there. Theoretical model for dielectric properties and discussions and analyses of the results are given in chapter 5. Finally in chapter 6, a paragraph of the conclusion is presented.

2 Theoretical Background of the Experiment

In this chapter, the basic concepts of dielectric constant and loss tangent are briefly reviewed. Then a formula for the loss tangent is derived for sapphire together with the measurement strategy of the surface resistance.

2.1 Definition of dielectric constant and loss tangent

Every material is electromagnetically characterized by its permittivity ϵ(F/m) magnetic permeability μ(H/m), and electrical conductivity σ(S/m). In a medium, the behaviour and propagation of electromagnetic wave are governed by Maxwell's equations and constitutive equations relating these properties to fields. The constitutive equations in a linear, homogeneous and isotropic material is given as:

$$\mathbf{D} = \epsilon \mathbf{E} \tag{2.1}$$

$$\mathbf{B} = \mu \mathbf{H} \tag{2.2}$$

$$\mathbf{J} = \sigma \mathbf{E} \tag{2.3}$$

where the dielectric displacement field $\mathbf{D}(C/m^2)$ is related to the electric field $\mathbf{E}$(V/m) by permittivity, the magnetic induction $\mathbf{B}(Wb/m^2)$ is related to the magnetic field $\mathbf{H}$(A/m) by the magnetic permeability and the current density $\mathbf{J}(A/m^2)$ is related to the electric field by the conductivity.

Equation (2.1) can also be written as

$$\mathbf{D} = \epsilon_0 \mathbf{E} + \mathbf{P} \tag{2.4}$$

where **P** is defined as the dipole moment per unit volume, which is related to the electric field as

$$\mathbf{P} = \epsilon_0 \chi_e \mathbf{E} \tag{2.5}$$

where ϵ_0 is the permittivity of vacuum and χ_e is the electric susceptibility. Then electric displacement field **D** is:

$$\mathbf{D} = \epsilon_0 (1 + \chi_e) \mathbf{E} \tag{2.6}$$

Relative permittivity or dielectric constant is defined as $(1 + \chi_e)$ and we denote it as ϵ'. For a linear material, the dipole moment induced by an external electric field **E** is proportional to **E**. If the electric properties of a material are independent of the direction of the external field, the material is isotropic. In an anisotropic material, the polarization induced by an external electric field in one direction is different from that induced in another direction. In this case, the electric susceptibility is a rank=2 tensor and so is the dielectric constant.

Now we take a look at Maxwell's curl equation in source-free medium for **H** in phasor form:

$$\nabla \times \mathbf{H} = j\omega \mathbf{D} + \mathbf{J} \tag{2.7}$$

According to (2.5), the definition of dielectric constant and equation (2.3), we can rewrite (2.7) as:

$$\nabla \times \mathbf{H} = j\omega\epsilon_0 (\epsilon' - j\frac{\sigma}{\omega\epsilon_0}) \mathbf{E} \tag{2.8}$$

We also have

$$\nabla \times \mathbf{E} = -j\omega\mu \mathbf{H} \tag{2.9}$$

We take a curl on both side of equation (2.9) and insert equation (2.8) and we get

$$\nabla \times (\nabla \times \mathbf{E}) = \omega^2 \mu\epsilon_0 (\epsilon' - j\frac{\sigma}{\omega\epsilon_0}) \mathbf{E} \tag{2.10}$$

together with

$$\nabla \cdot \mathbf{E} = 0 \tag{2.11}$$

we finally have:

$$\nabla^2 \mathbf{E} + \omega^2 \mu\epsilon_0 (\epsilon' - j\frac{\sigma}{\omega\epsilon_0}) \mathbf{E} = 0 \tag{2.12}$$

We can extract the complex wave number or complex propagation constant k as

$$k^2 = \omega\mu(\omega\epsilon - j\sigma) \tag{2.13}$$

In general, ϵ, μ and σ are complex quantities. If we neglect the magnetic properties and introduce imaginary parts ϵ'' and σ'', we need to rewrite k as

$$k^2 = \omega\mu[(\omega\epsilon' + \sigma'') - j(\omega\epsilon'' + \sigma')] \tag{2.14}$$

The loss tangent is then defined as

$$tan\delta = \frac{\omega\epsilon'' + \sigma}{\omega\epsilon' + \sigma''} \tag{2.15}$$

The real and imaginary parts of ϵ and σ have different physical meaning. However, in the dielectric measurements, we can not make distinctions between σ' and ϵ'' or between ϵ' and σ''[11]. We can also see in equation (2.14) that we can regard $\epsilon' + \sigma''/\omega$ as ϵ' and $\epsilon'' + \sigma'/\omega$ as ϵ''. Therefore, the most common form of $tan\delta$ is written as:

$$tan\delta = \frac{\epsilon''}{\epsilon'} \tag{2.16}$$

With the assumption $\epsilon'' \ll \epsilon'$, we take ϵ as purely real and use $\epsilon = \epsilon'$ instead of ϵ_r in this work. Note also that ϵ in general is dependent on frequency and temperature.

2.2 Derivation of formula of the loss tangent

The dielectric constant of the sapphire is a rank-2 tensor because it is not isotropic. If we set a rectangular coordinate system with z axis parallel to the c axis of the sapphire crystal (see figure 2.1), the dielectric constant tensor ϵ can be written as:

$$\epsilon = \begin{bmatrix} \epsilon_\perp & 0 & 0 \\ 0 & \epsilon_\perp & 0 \\ 0 & 0 & \epsilon_\parallel \end{bmatrix} \tag{2.17}$$

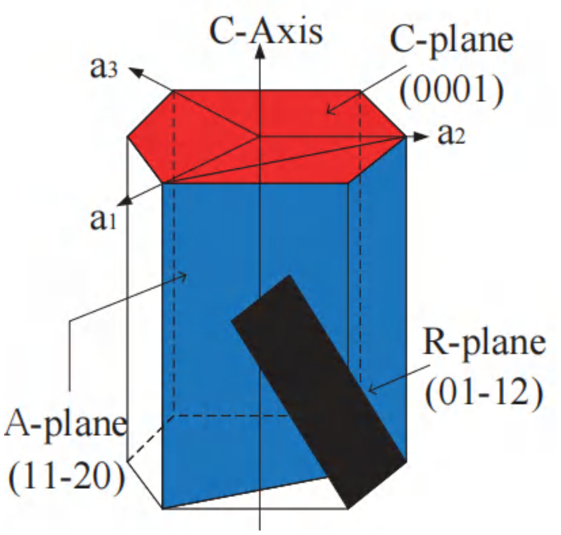

Figure 2.1: The crystal structure of sapphire[12].

In the experiment, we use a cylinder resonator containing a cylinder sapphire sample and we work in the cylinder coordinate system with the z axis and symmetric axis of resonator to be the same. We measure resonance frequencies f, which depends on both $\epsilon_\perp$ and $\epsilon_{||}$. However, for resonant modes for which the z component of electric field is small compared to the other components (quasi-TE mode), the effect of $\epsilon_{||}$ on resonance frequencies can be safely neglected. We use a simulation software called COMSOL to find the modes we have in the experiment. We adjust the value of $\epsilon_\perp$ until the resonance frequency is exactly the same as what we measure.

The measurement of the loss tangent depends on the quality factor Q. The quality factor is defined as 2π multiplied by the ratio of total energy stored in the system to the loss of energy per cycle:

$$Q = 2\pi \frac{U}{(W_d + W_c)T} \tag{2.18}$$

where U is the total stored energy, T is the period, W_d is power loss of dielectric material, sapphire in this case, and W_c is power loss of the conductor wall. Notice $T = 1/f$ and $2\pi f = \omega$, so we rewrite (2.18) as:

$$Q = \frac{\omega U}{W_d + W_c} \tag{2.19}$$

Assuming we have only the sapphire sample in the resonator, the total energy stored U in the system is given as:

$$U = \frac{\epsilon_0}{2}(\int_{V_{vac}} |\mathbf{E}|^2 dV + \int_{V_{samp}} \mathbf{E}^* \epsilon \mathbf{E} dV) \tag{2.20}$$

where $\mathbf{E}^*$ is the complex conjugate of $\mathbf{E}$, V_{vac} stands for the volume of region not occupied in the resonator and V_{samp} for volume occupied by the sapphire sample. We replace ϵ in (2.20) with (2.17) and get:

$$U = \frac{\epsilon_0}{2}(\int_{V_{vac}} |\mathbf{E}|^2 dV + \int_{V_{samp}} (\epsilon_\perp |E_\perp|^2 + \epsilon_\| |E_\||^2) dV) \tag{2.21}$$

where $E_\perp$ and $E_\|$ are the electric field components perpendicular and parallel to z axis respectively:

$$|E_\perp|^2 = |E_r|^2 + |E_\phi|^2 \tag{2.22}$$

$$|E_\||^2 = |E_z|^2 \tag{2.23}$$

The dielectric loss power is:

$$W_d = \frac{\omega\epsilon_0}{2} \int_{V_{samp}} (\epsilon''_\perp |E_\perp|^2 + \epsilon''_\| |E|^2_\|) dV \tag{2.24}$$

where $\epsilon''_\perp$ and $\epsilon''_\|$ are perpendicular and parallel component of the imaginary part of the complex dielectric constant. The power loss because of the conductor wall is:

$$W_c = \frac{1}{2} R_s \int_S |\mathbf{H}_t|^2 dS \tag{2.25}$$

where R_s is surface resistance of the wall, $\mathbf{H}_t$ is the component of $\mathbf{H}$ tangent to the wall and S stands for the all the surfaces of the wall. Since at resonance, the energy of magnetic field is equal to that of electric field, we can also write U as:

$$U = \frac{\mu_0}{2} \int_V |\mathbf{H}|^2 dV \tag{2.26}$$

The reciprocal of Q can be expressed as:

$$\frac{1}{Q} = \frac{W_d}{\omega U} + \frac{W_c}{\omega U} \tag{2.27}$$

We define:

$$U^\perp_{samp} = \frac{\epsilon_0}{2} \int_{V_{samp}} \epsilon_\perp |E_\perp|^2 dV \tag{2.28}$$

$$U^\|_{samp} = \frac{\epsilon_0}{2} \int_{V_{samp}} \epsilon_\| |E_\||^2 dV \tag{2.29}$$

$$U_{vac} = \frac{\epsilon_0}{2} \int_{V_{vac}} |\mathbf{E}|^2 dV \tag{2.30}$$

and notice that:

$$tan\delta_\perp = \frac{\epsilon''_\perp}{\epsilon_\perp} \tag{2.31}$$

$$tan\delta_{\parallel} = \frac{\epsilon''_{\parallel}}{\epsilon_{\parallel}} \tag{2.32}$$

Plugging these into (2.27) we get:

$$\frac{1}{Q} = \frac{U^{\perp}_{samp}}{U} tan\delta_{\perp} + \frac{U^{\parallel}_{samp}}{U} tan\delta_{\parallel} + R_s \frac{\int_S |\mathbf{H}_t|^2 dS}{\mu_0 \omega \int_V |\mathbf{H}|^2 dV} \tag{2.33}$$

We define the electric filling factors as:

$$P^{\perp}_{samp} = \frac{U^{\perp}_{samp}}{U} \tag{2.34}$$

$$P^{\parallel}_{samp} = \frac{U^{\parallel}_{samp}}{U} \tag{2.35}$$

$$G = \frac{\mu_0 \omega \int_V |\mathbf{H}|^2 dV}{\int_S |\mathbf{H}_t|^2 dS} \tag{2.36}$$

G is the geometric factor. Then (2.33) can be expressed as:

$$\frac{1}{Q} = P^{\perp}_{samp} tan\delta_{\perp} + P^{\parallel}_{samp} tan\delta_{\parallel} + \frac{R_s}{G} \tag{2.37}$$

We can see that the quantity $P_{samp} = P^{\perp}_{samp} + P^{\parallel}_{samp}$ is the ratio of the energy stored in the sample to the total energy. Notice that we have neglected the loss caused by air and water vapor in the whole deriving process. Details about it will be discussed later. In (2.37), all of the parameters are frequency dependent which means under a certain resonance frequency, we have one equation and two unknowns $tan\delta_{\perp}$ and $tan\delta_{\parallel}$. However, by selecting a mode for which $P^{\parallel}_{samp}$ is small compared to $P^{\perp}_{samp}$, in other words, E_z is small (quasi TE mode), we can neglect $P^{\parallel}_{samp}$ term and get:

$$tan\delta_{\perp} = \frac{1}{P^{\perp}_{samp}} (\frac{1}{Q} - \frac{R_s}{G}) \tag{2.38}$$

In addition, the real experiment include not only the sapphire sample in the resonator but also other materials whose dielectric properties are known. In this case, we just need to add extra terms in (2.37). More details will be discussed later.

In (2.37), Q can be acquired by experiment while $P^{\perp}_{samp}$, $P^{\parallel}_{samp}$ and G are calculated using COMSOL simulation. The only remaining parameter is the surface resistance of conductor walls. This can be acquired by doing an experiment with the empty resonator. For the empty resonator analytical solutions are obtained by applying Maxwell's equations. For example, for TE_{011} mode, Q is related to R_s as[13]:

$$Q = \frac{Z_0}{2R_s} \frac{(\frac{4\chi_{01}^2}{D^2} + \frac{\pi^2}{L^2})^{\frac{3}{2}}}{\frac{8\chi_{01}^2}{D^3} + \frac{2\pi^2}{L^3}} \tag{2.39}$$

where Z_0 is the wave impedance in free space with a value of 377 Ω. χ_{01} is the first zero of the derivative of the first-kind Bessel function. The strategy is that we measure the quality factor for a certain mode and then use (2.39) to get R_s. Since there is nothing in an empty resonator, there is no energy contained in the sample indicating $P_{samp}^{\perp}$ and $P_{samp}^{\|}$ are all zero. Thus equation (2.37) gives:

$$\frac{1}{Q} = \frac{R_s}{G} \tag{2.40}$$

This is equivalent to equation (2.39). G can be calculated analytically using (2.39) or using COMSOL. In the work by Breeze[13], a square root rule is stated for surface resistance that $R_S \propto \sqrt{f}$. Thus we can measure the surface resistance at one frequency point and at room temperature then we know it at any other frequencies. Experiments have been carried out to test this rule and the results are shown in chapter 4.

3 Experimental Setup and Measurements

In this chapter, we introduce the methods for the measurement of $\epsilon_\perp$ and $tan\delta_\perp$and mode identification. Various pictures of experimental setup and materials are also shown.

3.1 Dielectric measurements at room temperature

We use a cylinder resonator and a vector network analyser to get the resonance frequencies and unloaded quality factors for different modes. We start with the empty resonator to determine the surface resistance as described in the previous section and then we do measurements with the samples.

Figure 3.1 and figure 3.2 are the schematic and the photos of the resonator setup respectively. The resonator is made out of brass coated with silver. The inner part of the resonator is a hallow cylinder. There are two small channels connecting the inside and outside of the resonator located on the side wall of the resonator and opposite to each other, through which coupling cables are inserted. At the ends of the cables are two loops used to excite resonant modes. When the surfaces of loops are parallel to the bottom surface, hybrid mode with H_z component are excited. By adjusting the rotation of the semi-rigid high frequency cables, different modes can be excited. In order to keep the field mainly constrained in the sample and away from conductor walls of the resonator, we use a cylinder quartz to support the sample.

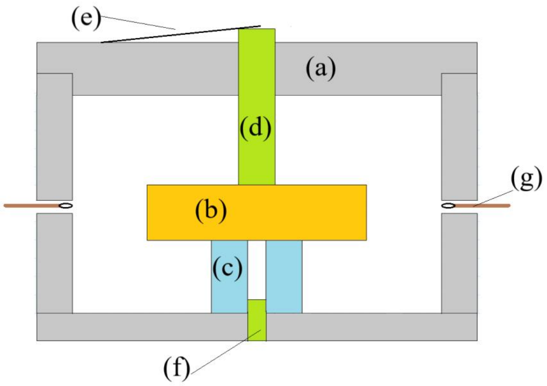

Figure 3.1: A schematic for the resonator (not-to-scale). (a) Top plate of the resonator; (b) the sapphire sample; (c) the quartz support; (d) the PTFE rod used to fix the sapphire sample; (e) a thin sheet metal spring; (f) the PTFE rod used to fix the quartz; (g) semi-rigid high frequency coupling cable to guide microwave and excite resonant modes

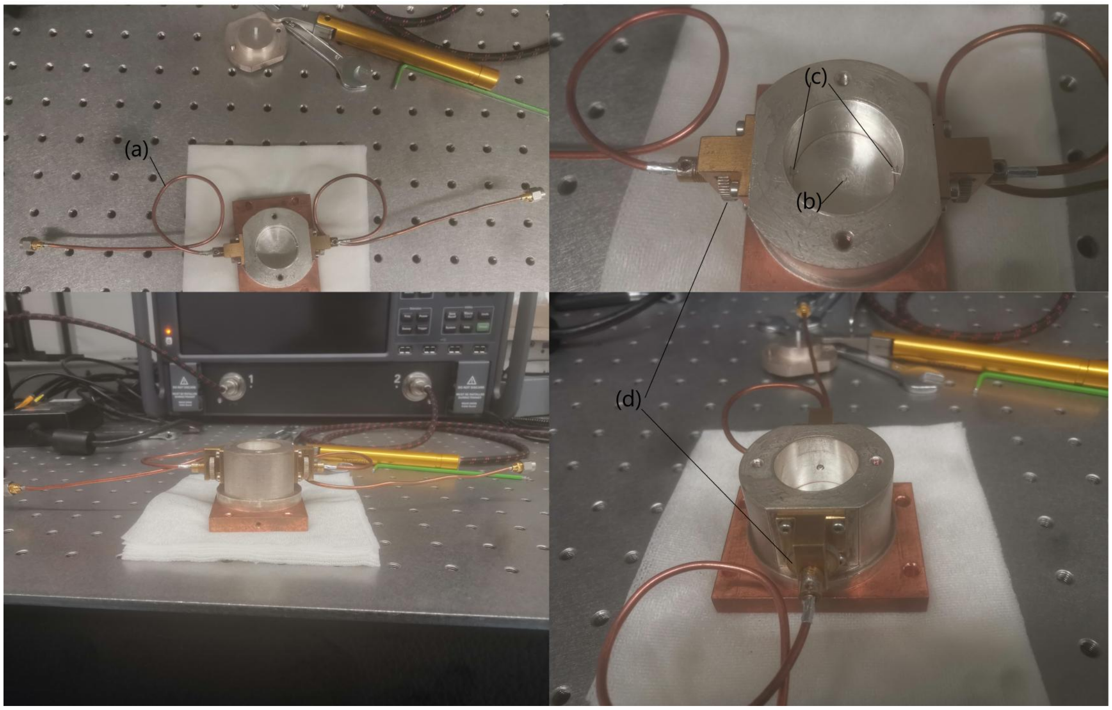

Figure 3.2: Real pictures for the resonator. (a) The cable ; (b) the PTFE rod used to fix the support at the bottom; (c) loops at the end of the cable to excite resonance modes; (d) the gear able to be rotated to adjust the distance between the loop and the symmetric axis of the resonator;

The quartz support is a hollow cylinder. To fix the quartz, we use a PTFE (short for polytetrafluoroethylene) rod as shown in figure 3.1. We need to put the cylinder sample also at the centre. In order to achieve this, a paper note with a certain width is cut with the help of vernier caliper.

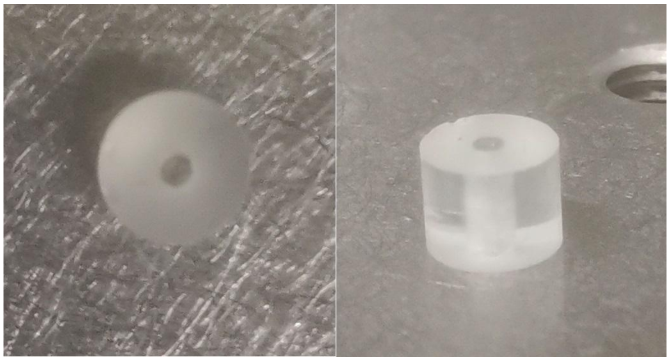

Figure 3.3: Photos of the quartz

After the sample is placed, this paper note is used to check if the distance between the edge of the samples and the wall of the resonator is equal to the width of the paper note at 8 different positions as shown in figure 3.4. This method centers the sample. Notice that one side of the paper should be closely attached to the wall of the resonator and the surface of paper should be through the center.

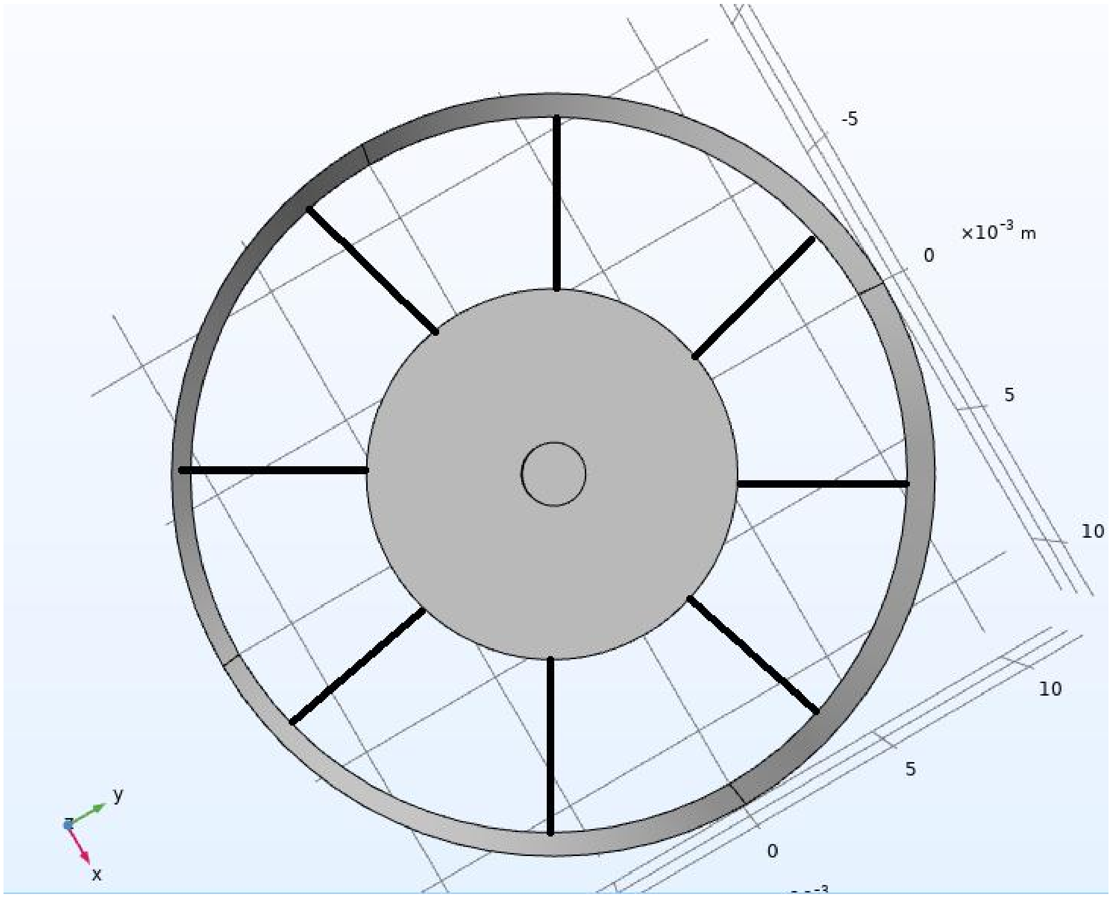

Figure 3.4: Top view of the schematic of the resonator set up. The paper note is inserted at 8 check positions.

In order to fix the sample, we use another PTFE rod inserted from the top. After we close the resonator, a thin sheet of metal spring is used on the PTFE to stabilize it in place (Figure 3.5). Outside the resonator, there are two gear knobs. By rotating these we can adjust the distance between loops.

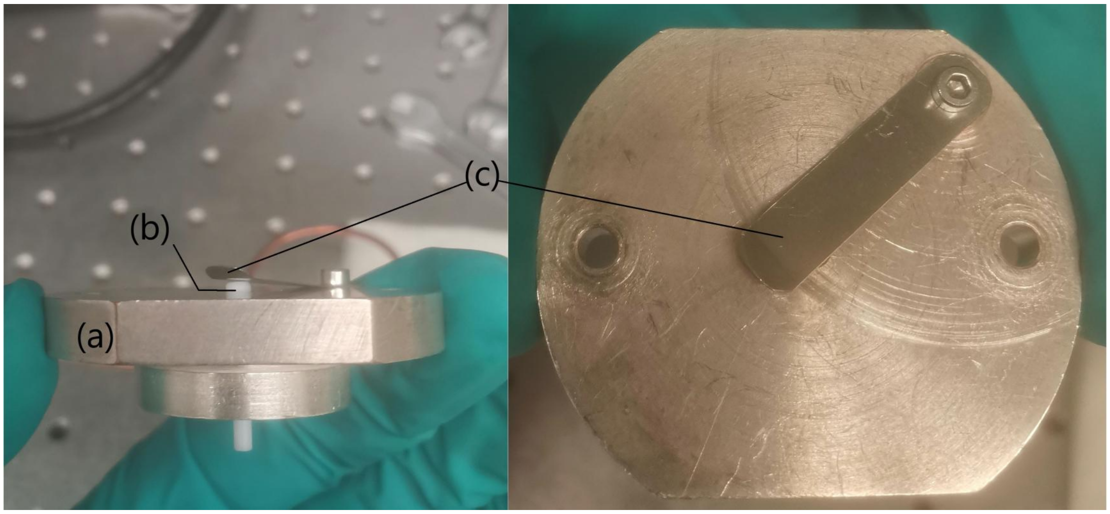

Figure 3.5: Photos of the top plate of the resonator. (a) The plate; (b) the PTFE rod used to fix the sample; (c) the thin sheet metal spring used to exert a force on the PTFE rod.

Six samples of sapphire have been used in the experiment. Three of them have a radius about 12 mm and height about 3 mm and the other three have a radius about 8 mm and height about 4 mm. The method of measuring the dimensions is presented later in section 3.6 and more precise dimensions are shown in section 4.1. In figure 3.6 a photo of one of these samples is shown. Samples are all of cylinder shape and have got a precise c axis cut (the upper and lower surfaces are perpendicular to the crystal c-axis). The cut precision of 8 mm samples are reported as 3°.

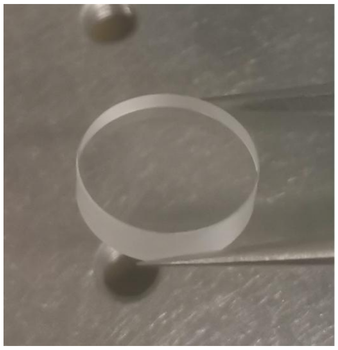

Figure 3.6: A photo of one of the sapphire samples

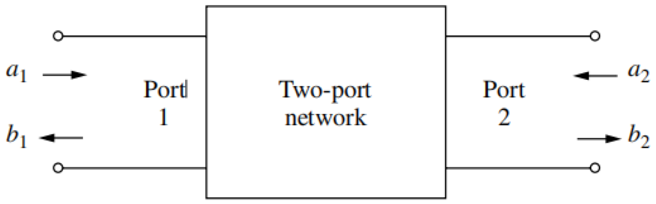

Figure 3.7: A two-port network

Another critical equipment used in the experiment is a vector network analyzer (VNA). A VNA can send microwave signal of different frequencies to a network and then receive the transmitted and reflected one to calculate the S parameters. The model number of the VNA is N5224B and produced by company Keysight. Its frequency range is 10 MHz-43.5 GHz. It has two ports connected to the semi-rigid high frequency cable. The resonator can be regarded as a two-port network as shown in figure 3.7 and the VNA measures the S parameters (S_{11}, S_{22} and S_{21}) of it. The S parameters are shown on the screen of the VNA in dB in frequency domain. S parameters describes the transmission and reflection of microwave power. If a_1 and a_2 stand for the power going into the network through port 1 and port 2 and b_1 and b_2 stand for the power leaving the network through port 1 and port 2, then the relationship between them and S parameters is given by

$$\begin{bmatrix} b_1 \\ b_2 \end{bmatrix} = \begin{bmatrix} S_{11} & S_{12} \\ S_{21} & S_{22} \end{bmatrix} \begin{bmatrix} a_1 \\ a_2 \end{bmatrix} \tag{3.1}$$

If a_i=0, we have

$$S_{jj} = \frac{b_j}{a_j}, (j = 1, 2) \tag{3.2}$$

$$S_{ij} = \frac{b_i}{a_j}, (j = 1, 2; i = 1, 2; j \neq i) \tag{3.3}$$

From equation (3.2) and (3.3), we can see that If we connect port j to a source and port i to a matching load, S_{jj} and S_{ij} are equal to the reflection coefficient at port j and transmission coefficient from port j to port i respectively.

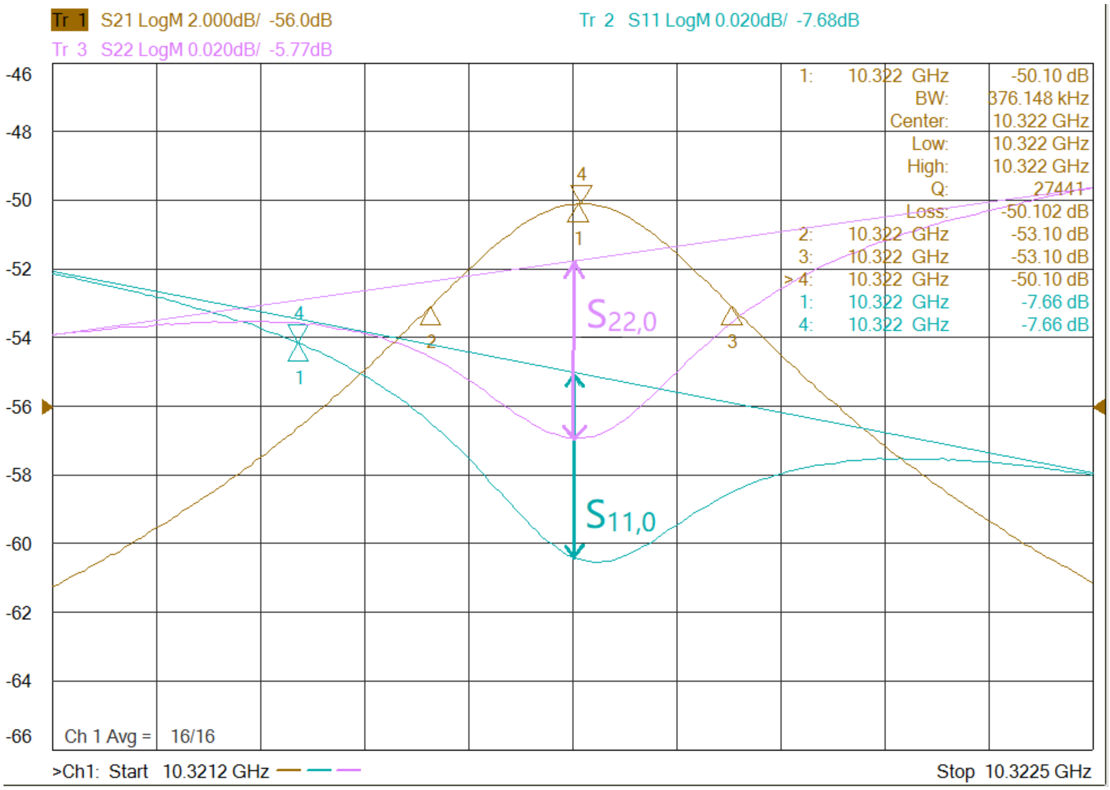

1:	10.322 GHz	-50.10 dB
	BW:	376.148 kHz
	Center:	10.322 GHz
	Low:	10.322 GHz
	High:	10.322 GHz
	Q:	27441
	Loss:	-50.102 dB
2:	10.322 GHz	-53.10 dB
3:	10.322 GHz	-53.10 dB
> 4:	10.322 GHz	-50.10 dB
1:	10.322 GHz	-7.66 dB
4:	10.322 GHz	-7.66 dB

Figure 3.8: An example measurement on one resonant frequency of the resonator

Figure 3.8 shows an example measurement where S_{21}(brown), S_{11}(blue curved line) and S_{22}(magenta curved line) are presented. S_{21} cone is Lorentzian. In addition, VNA also gives the -3 dB bandwidth Δf and displays the loaded quality factor Q_L of this mode by formula:

$$Q_L = \frac{f}{\Delta f} \tag{3.4}$$

We can see dips at the resonance point at S_{11} and S_{22} curves shown in figure 3.8. These dip values are denoted by $S_{11,0}$ and $S_{22,0}$ and used to calculate the coupling coefficients. The larger the coupling coefficients are, the larger the S_{21} is. We denote the coupling coefficient of port one and two as β_1 and β_2 respectively and then Q is given by[13]:

$$Q = (1 + \beta_1 + \beta_2)Q_L \tag{3.5}$$

Where β_1 and β_2 are coupling coefficients and given by

$$\beta_1 = \frac{1 - S_{11,0}}{S_{11,0} + S_{22,0}} \tag{3.6}$$

$$\beta_2 = \frac{1 - S_{22,0}}{S_{11,0} + S_{22,0}} \tag{3.7}$$

When doing measurement, we can set the frequency span shown on the screen, which we normally set 2.5-5 times as large as the bandwidth. We can also set how many points on one curve that VNA collect. The default number of points collected on one curve is 201, which is generally enough for the measurement. In addition, the number of average at each sample frequency is also an important parameter and a number of 16 is usually set to stabilize the measurement. We also need to lower S_{21} curve below -50 dB to achieve a weak coupling because if the coupling is too strong, the field configuration can be disturbed. But also it should not be too weak, or the noise would be non-negligible. By rotating the gears outside the resonator we can control coupling coefficients: The closer the loops are to the center, the larger the coupling coefficients are, or in other words, the larger the dips are. We want the dips to be equal to keep the symmetry of the whole setup. Finally, it is also worth to pay attention to the IF (intermediate frequency) Bandwidth. IF bandwidth is the bandwidth of the IF filter in the VNA. After the signal is received by the VNA, it is mixed with the signal generated by the local oscillator in a mixer and converted to the IF signal. Small bandwidth of IF filter means small portion of the signal is analysed each time. Therefore the smaller IF Bandwidth is, the more precise the measurement is and the more stable the curve is, though the longer it takes to finish the scan. IF Bandwidth should be much smaller than Lorentzian bandwidth. The typical value used is 5-10 kHz.

After setting everything properly, we can save the data as an s2p file and the screen as a png file. An s2p file records the frequency, the real and imaginary parts of all S parameters. Then the file is uploaded on a website called ARPE developed by Krkotic, Gallardo, Tagdulang, Pont and M. O'Callaghan. This website can extract unloaded and loaded quality factors, resonance frequencies and coupling coefficients from the S parameters in an s2p file and make plots (Figure 3.9). We briefly introduce the algorithm here and detailed information can be found in the paper[14]. First the algorithm recovers the asymmetries by repositioning S_{21} values in the complex plane to its theoretical position using

$$S_i' = S_i - \frac{S_1 + S_n}{2} \tag{3.8}$$

where S_i are measured values on VNA and S'_i are corresponding repositioned values. An initial coarse estimate of resonance frequency f_0 is made. Then the following equation, derived from circuit analysis of a lumped-element resonator, is used to fit the S'_i

$$S'_i = \frac{K}{1 + 2jQ_L(\delta_i - \delta_e) + G} \tag{3.9}$$

where K and G are complex fitting parameters, Q_L and δ_e are real fitting parameters and Q_L is the loaded quality factor. δ_i is given by

$$\delta_i = \frac{1}{2}(\frac{f_i}{f_0} - \frac{f_0}{f_i}) \tag{3.10}$$

Equation (3.9) is rewritten as:

$$F + 2jQ_L G\delta_i - 2jQ_L S'_i(\delta_i - \delta_e) = S'_i \tag{3.11}$$

This equation can be divided into real and imaginary parts and be written as a group of linear equations. There are 2n equations with 6 unknowns so these equations are overdetermined, which are solved using the Moore-Penrose inverse routines, which are better suited to perform the least-squares approximation. In addition, the algorithm also performs the removal of the outlier points by

$$\epsilon_i = |\frac{1}{S'_i - G} - \frac{K}{1 + 2jQ_L(\delta_i - \delta_e)}|^{-1} \tag{3.12}$$

The largest value of ϵ_i is compared to a threshold value

$$\epsilon_{max} < \frac{1}{Th|K|} \tag{3.13}$$

where Th is a threshold value defined as 10. If there are points with values of ϵ_i larger than $(Th|K|)^{-1}$, these points are deleted and the algorithm is repeated until (3.13) is valid.

For the extraction of $S_{11,0}$ and $S_{22,0}$, only data with $|Q_L|\delta_i \leqslant 0.5$ are used. The algorithm performs geometric least-squares fits of S_{11} and S_{22} in the complex plane and find out the complex centers (C_i) and radii (r_i). Then $S_{ii,0}(i = 1, 2)$ is given as

$$S_{ii,0} = \frac{||C_i| - r_i|}{|C_i| + r_i} \tag{3.14}$$

In addition, the algorithm gives the ratio of removed data to the total data, denoted by percentage of data removed (PDR).

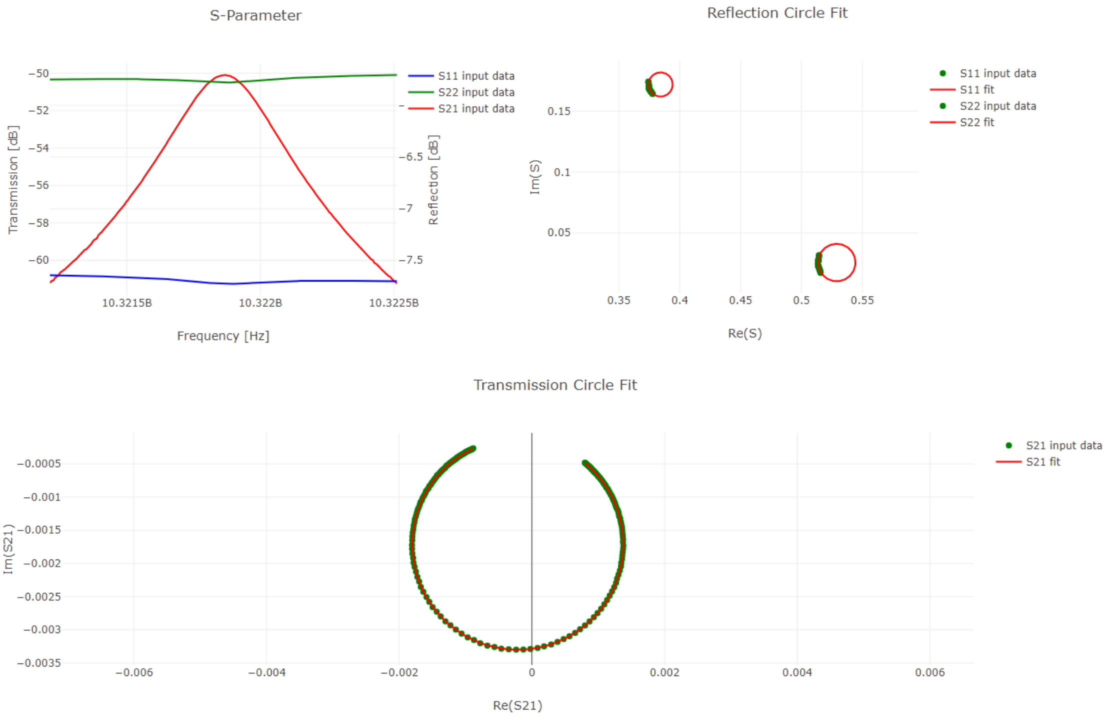

Figure 3.9: Plots of the example measurement made by ARPE. The S parameters are plotted in the frequency domain in the upper left plot. The other two plots show the circle fits of S parameters in the complex plane.

After the unloaded quality factor and resonance frequency are acquired, we use COMSOL to model the whole resonator setup, simulate the field configuration and find out the proper values of $\epsilon_{\perp}$ and $tan\delta_{\perp}$. Since the whole resonator setup is radially symmetric, we use a 2D cylindrically symmetric model as shown in figure 3.10 (i).

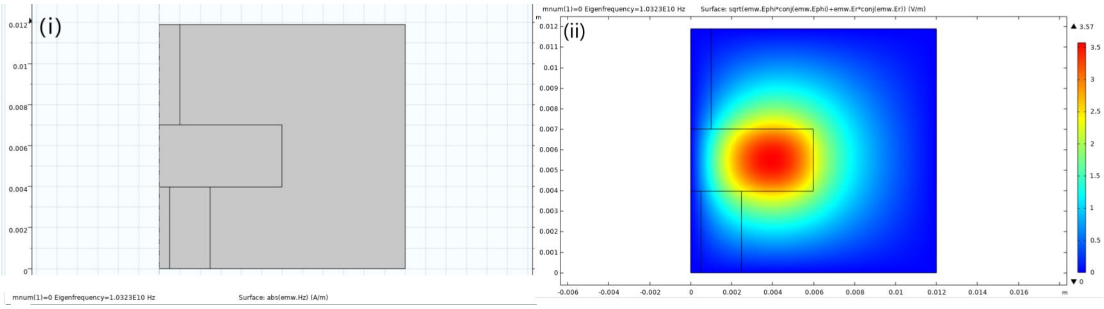

Figure 3.10: Screen shots from COMSOL. (i): The cross-section. (ii): E_{ϕ} for $TE_{01\delta}$ mode

COMSOL uses cylinder coordinate system and solves the following differential equations:

$$\nabla \times \mu_r^{-1}(\nabla \times \mathbf{E}) - k_0^2(\epsilon_r - \frac{j\sigma}{\omega\epsilon_0})\mathbf{E} = 0 \tag{3.15}$$

$$\mathbf{E}(r,\phi,z) = \tilde{\mathbf{E}}(r,z)e^{-im\phi} \tag{3.16}$$

where k_0 is the wave number in vacuum, m is called azimuthal number and μ_r, ϵ_r and σ are relative permeability, dielectric constant and conductivity respectively and their values are set by the user. Modes with m=0 are TE or TM modes while modes with m>0 are hybrid modes. We set μ_r=1 and σ=0. We use the values from literature for the dielectric properties of quartz[15] and PTFE[16]: $\epsilon^{\perp}_{quartz} = 4.44$, $\tan^{\perp}_{quartz} = 1.3 \times 10^{-5}$, $\epsilon_{PTFE} = 2.03$ and $tan\delta_{PTFE} = 2 \times 10^{-4}$. For sapphire, we can input a baseline value: $\epsilon_{\perp} = 9.36$ and $\epsilon_{\|} = 11.593$ at room temperature. After building the model and inputting proper values for the materials, simulation can be started to find out resonance frequencies and all the fields. COMSOL can give all of the possible modes but generally we just need to find out modes whose frequencies are close to what we get from VNA. Figure 3.10(ii) shows the simulation result of the example measurement. Since this is a TE mode, the E_z is zero and the field is mainly constrained in the sample. Thus dielectric properties of other materials and $\epsilon_{\|}$ have little effect on the measurement. We change the value of $\epsilon_{\perp}$ until the resonance frequency is the same as the measured one.

Next, we calculate $tan\delta_{\perp}$. Notice that we have not only the sapphire sample in the resonator but also quartz and PTFE, so two new terms are added into (2.37):

$$\frac{1}{Q} = P^{\perp}_{samp}tan\delta_{\perp} + P^{\|}_{samp}tan\delta_{\|} + P_s tan\delta_s + P_p tan\delta_p + \frac{R_s}{G} \tag{3.17}$$

Where P_s and P_p are energy filing factors for quartz and PTFE respectively and $tan\delta_s$ and $tan\delta_p$ are loss tangents. We neglect $P^{\|}_{samp}tan\delta_{\|}$ and get:

$$tan\delta_{\perp} = \frac{1}{P^{\perp}_{samp}}(\frac{1}{Q} - P_s tan\delta_s - P_p tan\delta_p - \frac{R_s}{G}) \tag{3.18}$$

Since we know the field configuration, we can calculate all integral-related quantities. COMSOL is able to calculate integral. The R_s is acquired from the empty resonator measurement. Then $tan\delta_{\perp}$ is the only unknown value.

What follows next is only the repetition of the above for different eigenmodes. First we find as many resonance modes as we can with VNA and extract the f and Q. After that, identify the modes on COMSOL and extract $\epsilon_{\perp}$. Then calculate $tan\delta_{\perp}$ in

COMSOL using (3.17). Finally $f - \epsilon_{\perp}$ and $f - tan\delta_{\perp}$ plots can be made, which are also important for the measurement of the parallel components. The steps of measurement of the parallel components are generally the same as perpendicular ones. One difference is that we need the modes with large E_z. To achieve this, we rotate the small loops in the resonator by 90 degree[13] to set it perpendicular to the bottom surface.

3.2 Cryogenic vacuum experiment

Since the MADMAX experiment will be conducted at a temperature around 4 K in vacuum to minimize the noise, it is important to perform the dielectric property measurements at cryogenic temperature. A cryostat is utilized to meet the requirement. A photo of the cryostat is shown in figure 3.11. The vacuum chamber is of radius of 78.55 mm and the round mounting cold plate fits the chamber. The resonator is placed on the mounting cold plate of the cryostat using a copper structure in upright direction. Temperature probes (Figure 3.12) are located on the mounting plate and on the copper structure. A high frequency (2.92 mm/Type K, part #CF40-2-SMA50-40GHz) SMA vacuum feed through on a flage CF40 from VACOM is used to connect the resonator to the VNA through one of the ports of the cryostat.

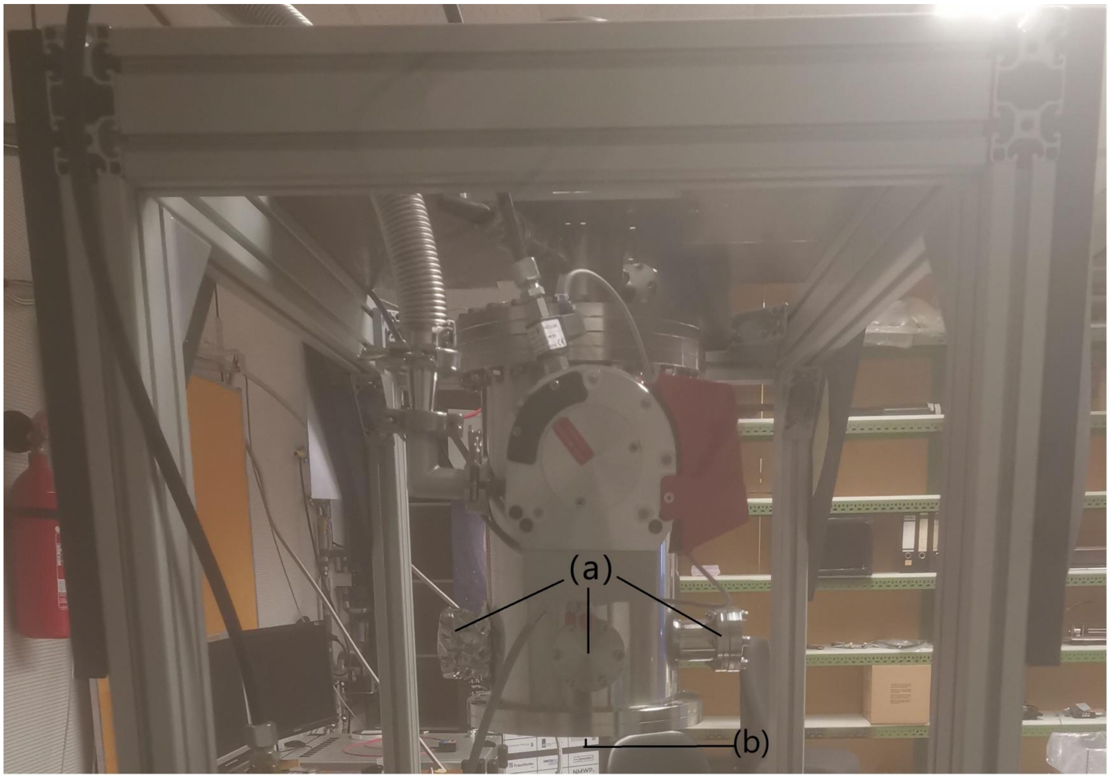

Figure 3.11: The cryostat. (a) Ports of the cryostat. (b)CF 100 access port

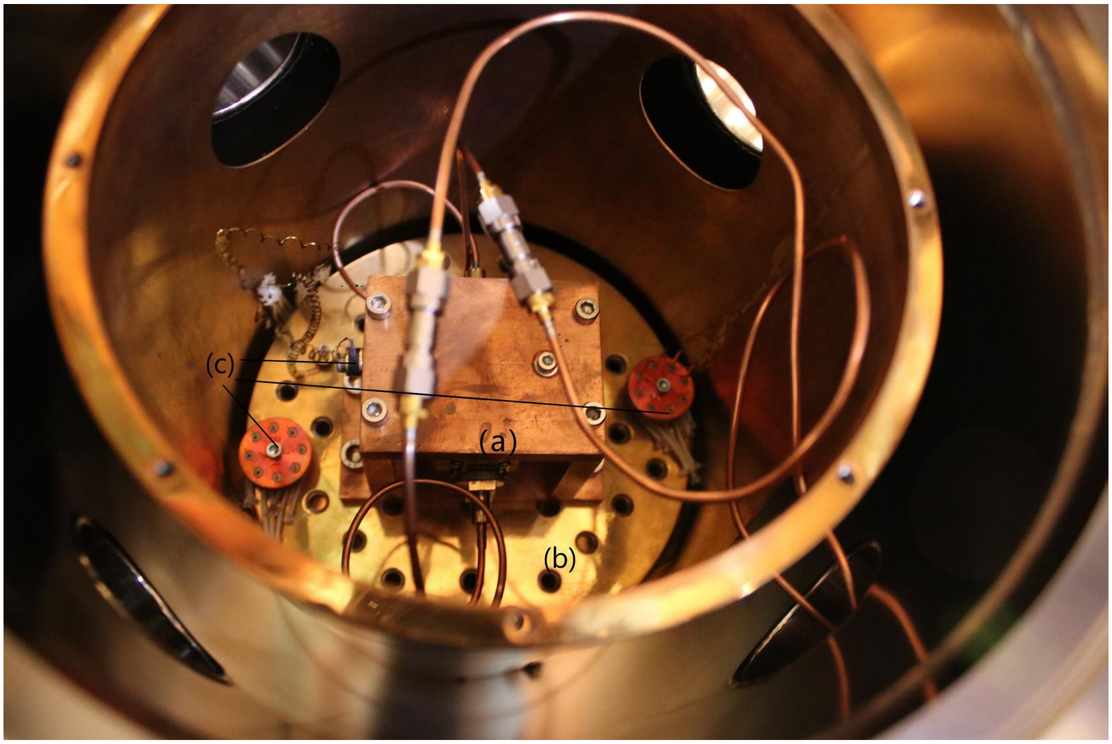

Figure 3.12: A photo of the inner part of the cryostat. (a) Copper mount of the resonator; (b) cold mounting plate; (c) temperature probes

3.3 Uncertainties

All measurements are inevitably accompanied by uncertainties. Generally, the results of measurement on $\epsilon_\perp$ is dependent on a series of independent parameters p_i. In this thesis, standard deviation σ is used to represent the uncertainty. Uncertainty of $\epsilon_\perp$ can be expressed as:

$$\sigma_{\epsilon_\perp} = \sqrt{\sum_i^n (\frac{\partial \epsilon_\perp}{\partial p_i} \sigma_{p_i})^2} \tag{3.19}$$

where σ_{p_i} is the uncertainty of the corresponding parameter. For $\epsilon_\perp$, these parameters are the radius and height of the resonator (R_{res} and H_{res}), the radius and height of samples (R_{samp} and H_{samp}) and the resonance frequency we get for a certain mode. For $tan\delta_\perp$, these parameters are Q and R_s. In order to work out the uncertainties, multiple measurements on each parameter have been conducted. Then an average value and standard deviation are acquired by:

$$\bar{x} = \frac{x_1 + x_2 + \cdots + x_n}{n} \tag{3.20}$$

$$\sigma_x = \sqrt{\frac{\sum(x_i - \bar{x})^2}{n-1}} \tag{3.21}$$

where n is the number of measurements, x_i is measurement value each time. For partial derivative of $\epsilon_\perp$, each related parameters is scanned in the range $[\bar{x} - \sigma_x, \bar{x} + \sigma_x]$ in COMSOL and for each parameter value we repeat the process of simulation in section 3.2 so that we have an $\epsilon_\perp$-x plot and then a function fit can be made to get the partial derivative at the average value. For partial derivatives of $tan\delta_\perp$, we use (3.17) and get:

$$\frac{\partial tan\delta_\perp}{\partial Q} = -\frac{1}{P_{samp}^\perp Q^2} \tag{3.22}$$

$$\frac{\partial tan\delta_\perp}{\partial R_s} = \frac{1}{P_{samp}^\perp G} \tag{3.23}$$

G and $P_{samp}^\perp$ can be got from COMSOL simulation and then we have everything needed in (3.19)

3.4 Effect of air and square root rule test

When room temperature experiment is carried on, the dielectric properties of air can be another cause of error. In equation (3.17) and the whole simulation process, we suppose that the dielectric constant and loss tangent of air are 1 and 0 respectively. Besides, water vapor could also have an effect on results. For dielectric constant of air, a typical value of 1.00058986±0.0000005 is measured by Hector and Schultz[17].

For loss tangent of air, we use an atmospheric absorption model proposed by Wentz and Meissner[18]. In their work, the relation between the absorption coefficient of dry air α_D and water vapor α_V and frequency f has been studied. The frequency range they investigate is 0-100 GHz. If we only focus on 10-40 GHz, α_D increases gradually from about $2 \times 10^{-6}\ m^{-1}$ to $1.3 \times 10^{-5}\ m^{-1}$ while α_V goes up to a maximum of about $3.4 \times 10^{-5}\ m^{-1}$ around 22 GHz and then drops to $1.5 \times 10^{-5}\ m^{-1}$. According to the definition of the absorption coefficient, we have:

$$\alpha = 2|Im(k)| \tag{3.24}$$

where k is the wave number given as:

$$k = \omega\sqrt{\mu_0\epsilon_0\epsilon_r(1 + itan\delta)} \tag{3.25}$$

Generally, the loss tangent is much smaller than 1 so we have:

$$\sqrt{1 + itan\delta} \approx 1 + \frac{1}{2}itan\delta \tag{3.26}$$

Notice that $1/\sqrt{\mu_0\epsilon_0} = c$, where c is the speed of light in vacuum. Now equation (3.24) is written as:

$$tan\delta = \frac{\alpha c}{2\pi f\sqrt{\epsilon_r}} \tag{3.27}$$

With (3.27) we can estimate the loss tangents of air or water vapor. Both α_D and α_V are smaller than $4 \times 10^{-5}\ m^{-1}$ in 10-40 GHz, so we set $\alpha = 4 \times 10^{-5}\ m^{-1}$ in (3.27) and when $f = 10$ GHz, loss tangent is about 2×10^{-7}. Compared with the typical value of $tan\delta_\perp \approx 10^{-5}$, this effect can be neglected.

To estimate the effect caused by air, we also conduct an experiment. The cryostat vacuum chamber is used at room temperature. Then we compare the results with those acquired in the normal laboratory environment to see how much the effect of air and water vapor is. In addition, an experiment is also carried out in nitrogen. Since the nitrogen available is dry, we can observe the effect of water vapor alone.

A glove bag (AtmosBag from Sigma-Aldrich) shown in figure 3.13 is used for this nitrogen experiment. The resonator is sealed in and connected to the VNA through the glove bag inlets. We fill the bag with nitrogen and flush, and then repeat this process three times to effectively reduce the air in the bag. The nitrogen experiments are carried only for the empty resonator, whose results are compared to the aired ones to check if there is any difference.

These experiments are done with the empty resonator at different resonance modes, so we can also check by the way if the square root rule is valid under different environment. By looking at equation (3.17), if the G factor is large enough, the $\frac{R_s}{G}$ term can be neglected. Thus if we want to minimize the effect of R_s, we can use modes with high G.

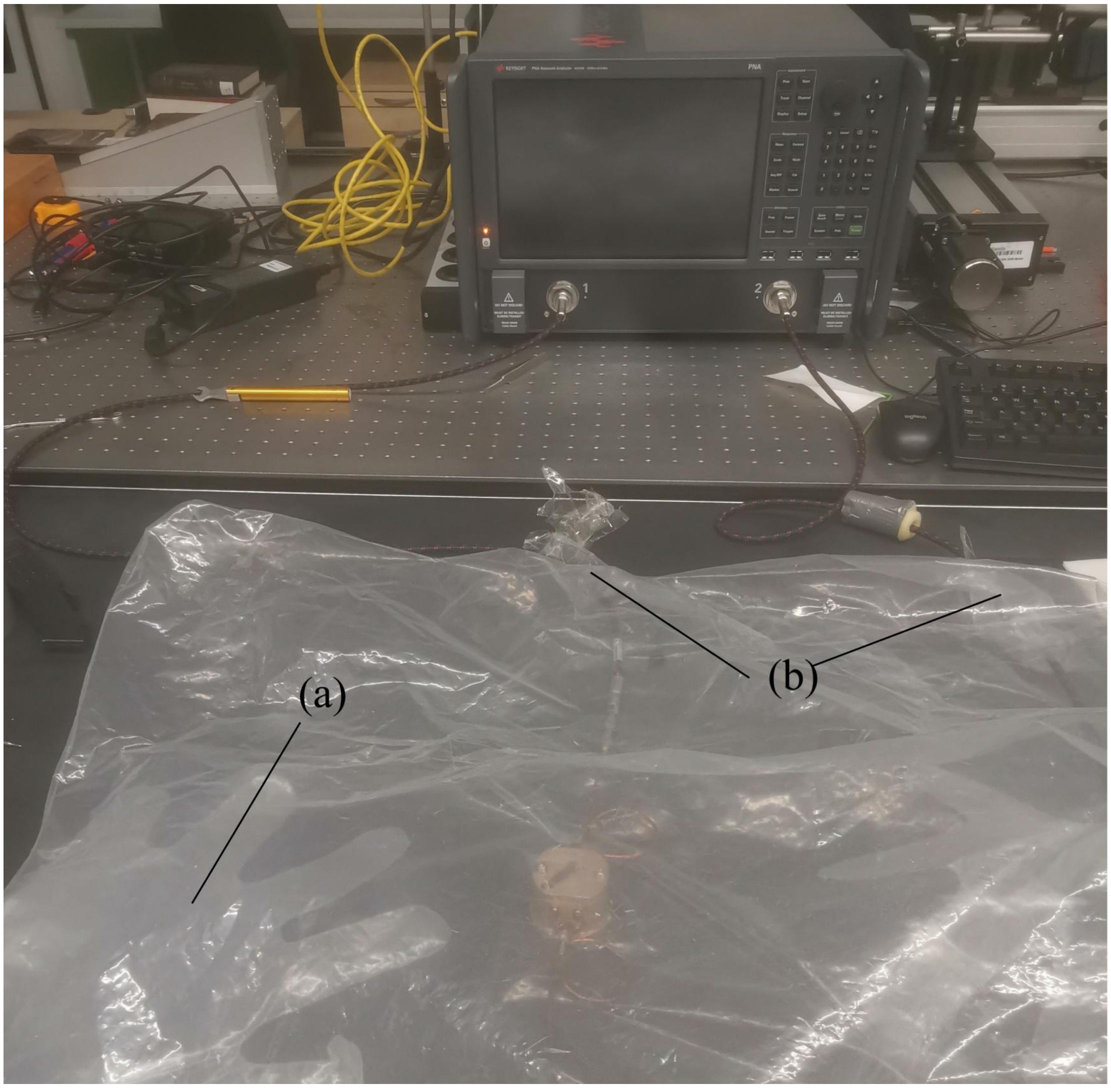

Figure 3.13: The glove bag (AtmosBag from Sigma-Aldrich) used in the nitrogen experiment. (a) the inner glove; (b) two ports

3.5 Mode identification

Multiple modes exist near a given frequency and in some cases they are so close that a priority knowledge of possible epsilon range is not enough to identify the correct mode. Luckily, simulations on COMSOL show that generally different modes have different response to positioning of the sample. The increment or decrement in frequency per 100 μm between modes varies, which helps us identify the correct mode. In this way, errors caused by mode identification can be avoided.

Consequently, more paper notes are made to make sample deviate from the center (Figure 3.14). These papers allow us to control the deviation distance from the center by steps of 250 μm. In practice, it is hard to make accurate steps of 250 μm so only 500 μm and 1 mm deviations are conducted in the resonator and on COMSOL and difference in frequencies with and without deviation is recorded as $\Delta f_{comsol/vna} = f_{shifted} - f_{centered}$. Notice that we cannot use a 2D model in COMSOL since the whole system is not cylindrically symmetric anymore if we deviate samples from the center. However, it still has one symmetric plane parallel to the direction of deviation and through the center. Thus one-half 3D model is built in COMSOL for computational efficiency as shown in figure 3.15. We input the values of dielectric properties of sapphire and deviate the sample from the center by also 500 μm or 1mm to get Δf_{comsol}. Then the same thing can be done to get Δf_{VNA} and then we compare these two. If for a certain mode, these two differences are close then to some extent we can say we have matched a proper mode on COMSOL with that we have on VNA. If not, other modes on COMSOL need to be considered.

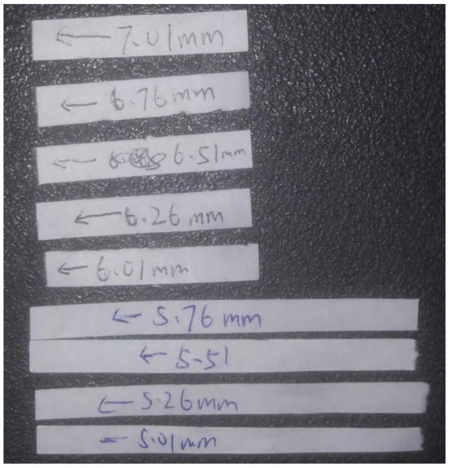

Figure 3.14: Groups of paper notes with steps of 0.25 mm. The 6.01 mm one is used to center the 12 mm samples and others are used to deviate the sample. For example, the 6.26 mm and 5.76mm are used to shift the sample from center by 0.25 mm. The arrows on paper indicate the right sides supposed to be inserted because the parallel cut cannot be guaranteed

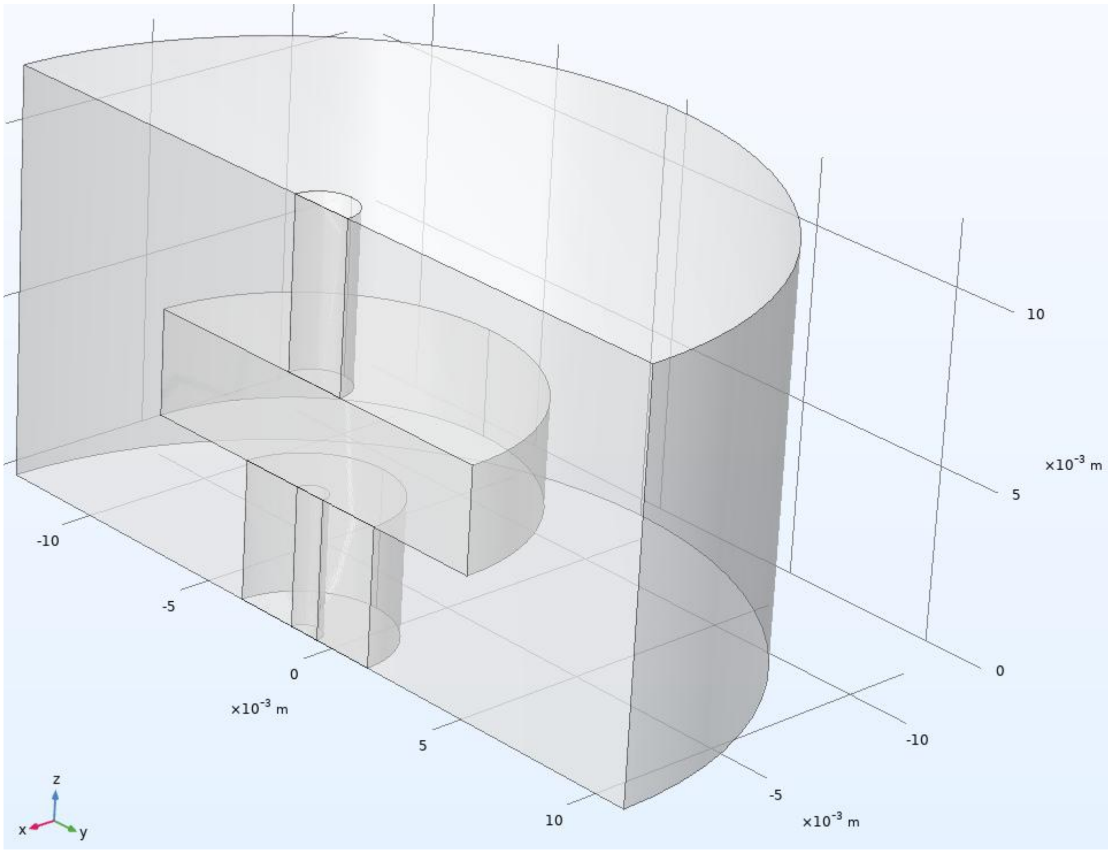

Figure 3.15: One half of the 3D model in COMSOL

In addition, we can also achieve mode identification by comparing the difference with and without the PTFE rod. First we do the normal measurement and we get a resonance frequency f and then we remove the PTFE rod and do the same thing to get the resonance frequency f'. Then we calculate $\Delta f_{vna} = f' - f$. Similarly, we can also get $\Delta f_{comsol} = f' - f$ in the simulation and again we compare Δf_{vna} with Δf_{comsol}. The advantage of this method is that it is much easier to operate on the resonator and a 3D model is no longer needed but since the PTFE rod is used to hold the sample at the center, the removal of it is after any other operation on the resonator. Both methods are employed to the mode identification in practice.

3.6 Measurement of dimensions

It is important to know the dimensions of materials and the resonator to build an accurate model in COMSOL. A micrometer as shown in figure 3.16 is used for the measurement of the radius and the height of sapphire samples. The precision is 0.001 mm. First we do a measurement with nothing between the measuring faces. We rotate the thimble and then rotate the ratchet knob when the two faces are very close. We stop rotating rightly after the two faces touch each other and write down the reading D_0. Afterwards we measure the dimension of a sample and write down another reading D. Then $D - D_0$ is recorded as the result of the measurement.

Figure 3.16: The micrometer used in the lab

Figure 3.17 is the photos of another micrometer for inner radius measurements for the resonator. The range is 20-25 mm and the precision is 0.005 mm. By rotating the ratchet, we can control those three anvils at the bottom until they touches the inner walls of the measured object. First we measure the diameter of the set ring shown in figure 3.18 and write down the reading r_0. Though the diameter of this set ring exceeds the range by 13 μm at 293 K, the extra part can still be measured by reading the thimble. If r_0 is not equal to the diameter of the set ring, datum point setting needs to be done. Then we measure the diameter of the resonator. Since our lab temperature is usually 2-4 K higher than 293 K, an assumption is made that the change in diameter of the set ring can be neglected.

Figure 3.17: The micrometer for the inner radius measurement(left) and three anvils at the bottom(right)

Figure 3.18: The set ring with a diameter 25 mm+13 μm at 293 K

We use a depth micrometer to measure the height of the inner space of the resonator. Figure 3.19 shows photos of the depth diameter. There is a moving spindle in the measuring face. We can control the length of the standing-out part of the spindle by rotating the ratchet. The reading is shown on the screen, which has a precision of 0.001 mm. First, we let the micrometer stand on its measuring face on a hard clean flat and rotate the ratchet until the spindle gently touches the surface. We press and hold the 'SET' button to set the datum point. After that we can start the measurement.

Figure 3.19: The depth micrometer(left) and the moving spindle at the bottom(right)

We measure each dimension 10-20 times and calculate the mean value and the one-standard deviation according to equation (3.20) and (3.21) and record the temperatures. In addition, all of the measuring surfaces and measured objects should be clean during the measurement. Measured values of dimensions are shown in section 4.1. Finally, we use the temperature dependence[19] of dimensions of the resonator and sapphire to calculate dimensions of the resonator and samples at 18 K.

4 Results

In this chapter, we show the results of the experiments mentioned in the previous chapter. Various plots and tables are presented and data from other literature are also cited to make a comparison.

4.1 Dimensions of sapphire samples and the resonator

Table 4.1 shows the dimensions of the sapphire samples and the resonator and temperatures when doing measurement. The results of dimensions are presented as the mean value plus and minus one standard deviation, which are calculated using equation (3.20) and (3.21) in section 3.3. Here we name those three sapphire samples with a diameter of 12 mm as sample 1,2 and 3 and the other three with a diameter of 8 mm as sample 4, 5 and 6. The samples vary slightly in both diameter and height. Samples of 8 mm group have a larger range for both dimensions compared with those of 12 mm group. As for the resonator, the height varies larger than diameter. The measurement temperature of the radius is 296.5 K and of the height is 295.3 K. The radii of PTFE rod and quartz support are 1 mm and 2.48 mm respectively. The height of quartz is 3.98 mm and its inner radius is 0.503 mm. As we mentioned previously, the electromagnetic field is mainly constrained in the sample, so the dimensions of PTFE rod and quartz support have much less effect on the measurement results. Thus we do not take into account their uncertainties in dimensions as what have been done for others.

Item	Diameter(mm)	Height(mm)	temperature(K)
sample 1	11.970±0.001	3.017±0.0015	296.9
sample 2	11.967±0.001	3.024±0.0005	296.5
sample 3	11.970±0.0015	3.027±0.001	296.5
sample 4	8.089±0.0025	4.028±0.001	295.4
sample 5	8.019±0.003	4.025±0.0005	296.6
sample 6	8.045±0.0025	4.002±0.0005	295.1
Resonator	24.0036±0.001	11.899±0.0035	296.5, 295.3

Table 4.1: Dimensions of the samples and the resonator and measured temperatures. The dimension values are the mean value plus/minus one standard deviation.

4.2 Results of square root rule test and experiments in nitrogen and vacuum at room temperature

The results of surface resistance measured in air, nitrogen and vacuum are shown in figure 4.1 and we can see the results of them are all close enough to each other, which indicates that the air and the water vapor have little effect on the measurement of R_s. A power fit (of form af^b) is made (purple line) with the help of Matlab's curve fitting tool giving $Rs \propto f^{0.5216}$, about 4 percent larger than 0.5. In addition, other two square root rule (SRR) lines are plotted, scaled at 42 GHz and 29 GHz respectively. From the plot, we use one half of the maximum of difference between the green line and the blue line as the uncertainty σ_{R_s}, which is about 3 $m\Omega$.

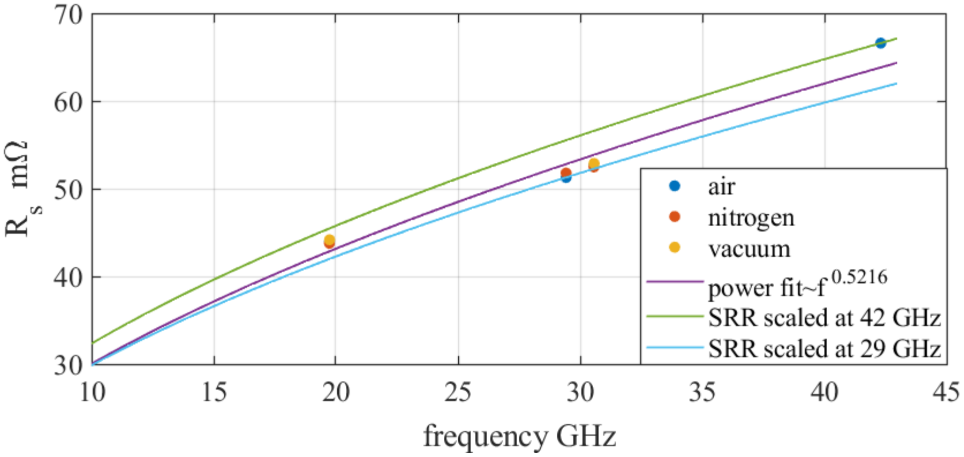

Figure 4.1: surface resistance in air , nitrogen and vacuum at room temperature

Actually, square root rule is based on the following definition:

$$R_s = \sqrt{\frac{\pi f \mu_0}{\sigma}} \tag{4.1}$$

where σ is electrical conductivity and is regarded as a constant, However, it can also depend on the frequency, which may explain a part of 4% relative error in the power fit.

In addition, during the experiment, we find the resonance frequency of the TE_{01} mode is changing when the pressure goes down, which is recorded in figure 4.2, though the change is only 6 MHz. The temperature recorded at 10^3 hPa is 300 K and goes down to 299.66 K at 10^{-4} hPa. Thus this 6 MHz difference can be caused by the change of temperature.

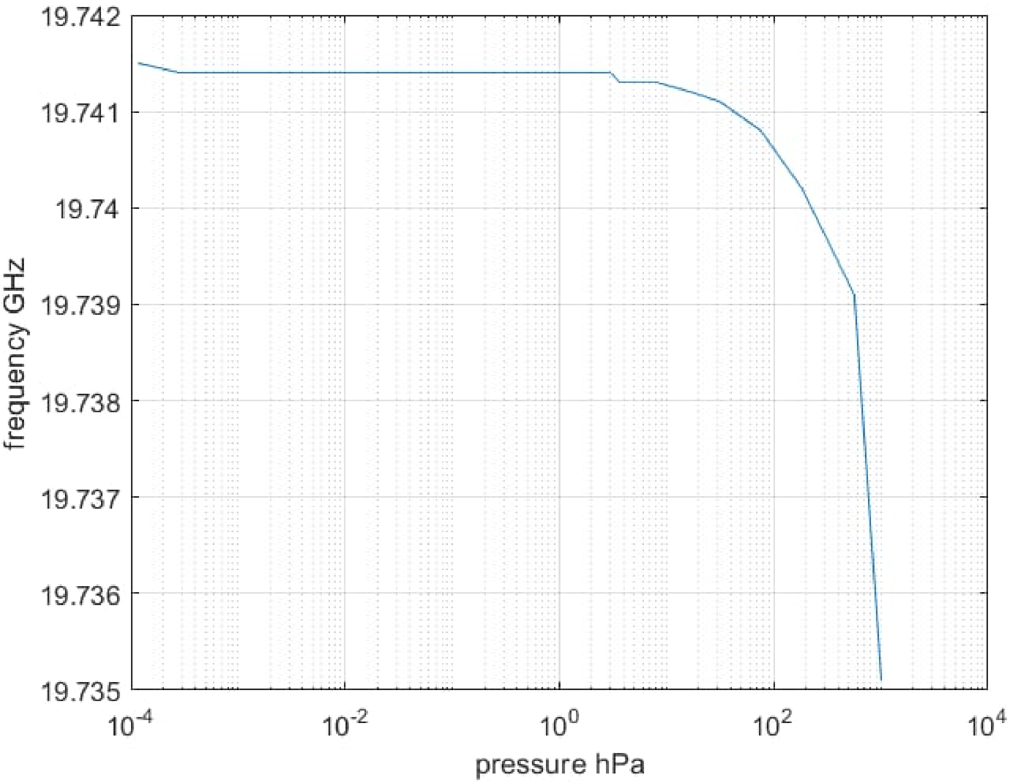

Figure 4.2: Plot of resonance frequency versus pressure at room temperature

4.3 Perpendicular components of dielectric properties at 295-297 K

We use the square root rule scaled at 19.73GHz, at which the R_s is 43.8 $m\Omega$. Thus over the whole frequency span we have

$$R_s = 43.8m\Omega \times \sqrt{\frac{f(GHz)}{19.73}} \tag{4.2}$$

Figure 4.3 and figure 4.4 shows $\epsilon_\perp$ as a function of frequency for 12 mm and 8 mm samples respectively. Combined data is shown later in figure 4.8. Detailed data like G, $P^{\perp}_{samp}$ and percentage of data removed mentioned in section 3.1 are shown from table 4.2 to table 4.7. We only collect percentage of data removed (PDR) for only one sample in each sample group. One thing that can be immediately noticed for $\epsilon_\perp$ from figures is that both groups of samples have a peak, though at different frequencies. The range of

$\epsilon_\perp$ axis is 0.12, which means that the fluctuation is within 1.3%, so the dependence on frequency is not so strong. In each group, the values of the three samples at the same frequency are close. In addition, if we ignore the peak, $\epsilon_\perp$ is almost constant between 10 GHz and 40 GHz for 12 mm samples. For 8 mm groups, it climbs gently up to 42 GHz.

In section 2.2 we have mentioned that the resonant frequency is dependent on both $\epsilon_\perp$ and $\epsilon_{||}$ and we need to choose those modes with negligible E_z so that the dependence on $\epsilon_{||}$ can be safely neglected. According to equation (2.28), (2.29), (2.34) and (2.35), this means choosing modes with negligible $P^{||}_{samp}$ compared with $P^{\perp}_{samp}$. From table 4.2 to table 4.7 we can see that all $P^{||}_{samp}$ are small enough compared with $P^{\perp}_{samp}$, so these modes are good for the perpendicular component measurement. The modes with m=0 are TE modes so there is no E_z component, which leads to $P^{||}_{samp}$=0. Most of $P_{samp}(= P^{||}_{samp} + P^{\perp}_{samp})$ are above 0.7 so the field is mostly confined in the samples. For modes of 23.8 GHz and 27.6 GHz of 12 mm samples and at 21 GHz of 8 mm samples, the filling factor P_{samp} is low compared to other resonances and these points deviate from the overall trend, which therefore indicates the effect of the permittivity is less and the apparent deviation is most likely caused by some other parameters. If we ignore these points, $\epsilon_\perp$ is almost constant in this frequency range. In addition, most of PDR are small while that of 33.05 GHz mode of sample 3 is almost one half.

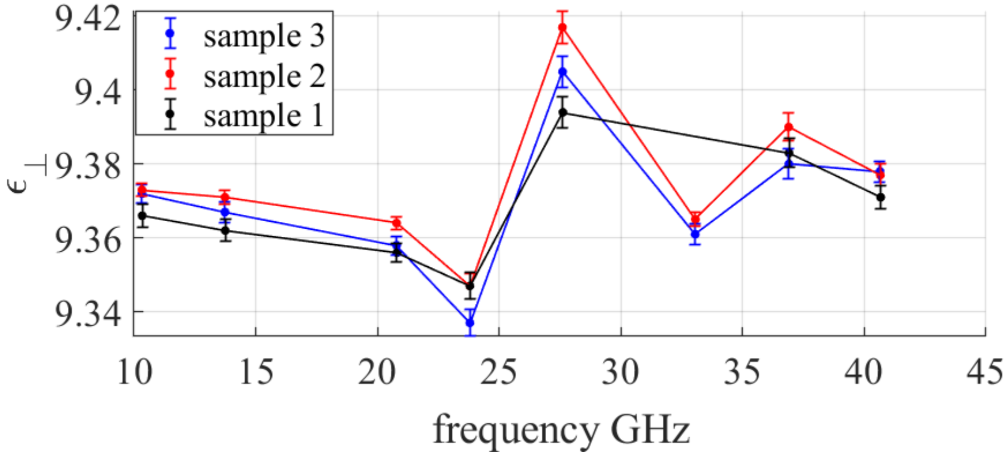

Figure 4.3: perpendicular components of dielectric constant versus frequency for the 12 mm samples at room temperature

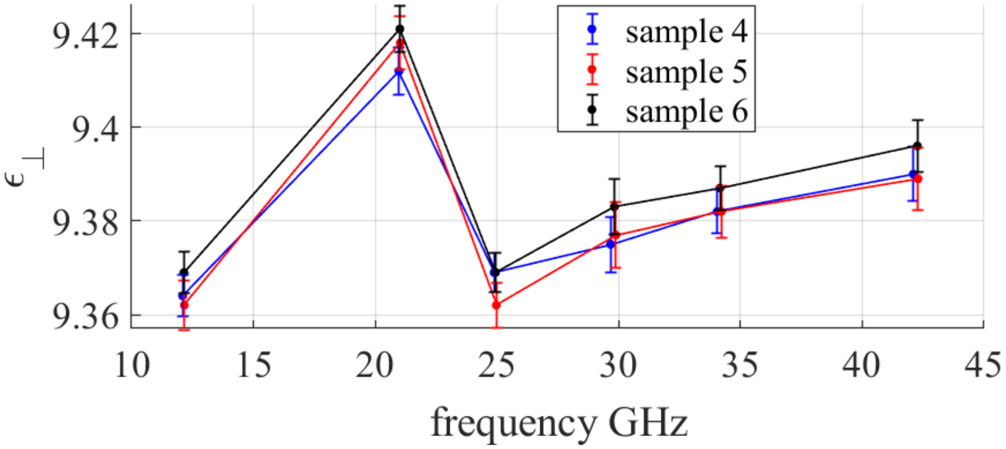

Figure 4.4: perpendicular components of dielectric constant versus frequency for the 8 mm samples at room temperature

To see how well the Lorentzian curves look, we use our own Lorentzian fit code in Matlab. We have fitted data of 10.3 GHz mode (high $P^{\perp}_{samp}$ and low PDR), 27.5 GHz and 20.9 GHz modes (low $P^{\perp}_{samp}$ and low PDR) and 33 GHz (high $P^{\perp}_{samp}$ and high PDR). Results are shown in figure 4.5. The χ^2 is defined as

$$\chi^2 = \frac{\sum\limits_i (y_i' - y_i)^2}{\sum\limits_i y_i^2} \tag{4.3}$$

Where y_i' is each fitted value and y_i is each measured value. The smaller the χ^2 is, the better the Lorentzian fit is. We see that 10.3 GHz mode has the smallest χ^2. 27.5 and 33 GHz modes have a much larger χ^2. So we can see that the Lorentzian fit sometimes is not so good for modes with high PDR or low $P^{\perp}_{samp}$.

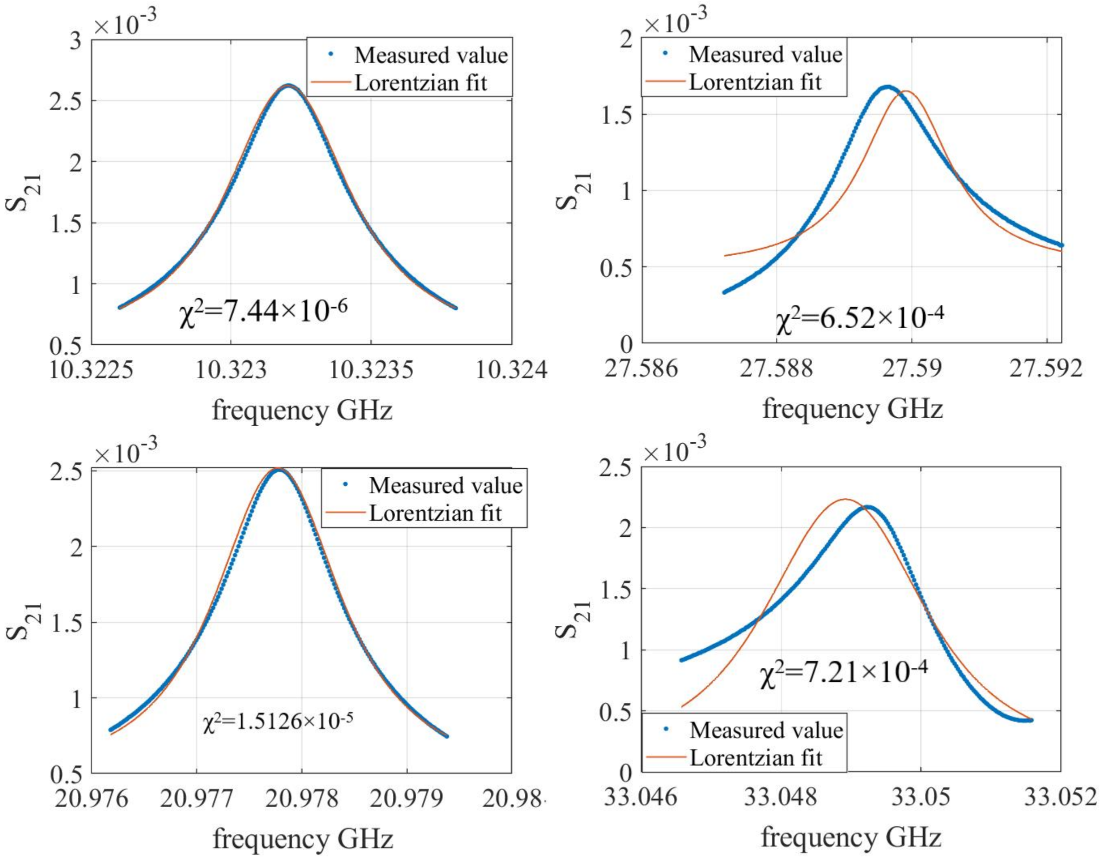

Figure 4.5: Lorentzian fits for 10, 27, 24 and 33 GHz modes

Figure 4.6 and figure 4.7 show $tan\delta_\perp$ results for 12 mm and 8 mm samples respectively. Combined data is shown later in figure 4.9. Generally speaking, for both groups of samples, it increases gradually from 1×10^{-5} at 10 GHz to about 7×10^{-5} at 42 GHz. In each group, the values of the three samples are still close at the same frequency. From table 4.2 to table 4.7 we see that most G factors are a few thousands. If we calculate R_S/G, most of them are about 10^{-5}, comparable with $tan\delta_\perp$, so they can not be neglected. Thus for these modes, the proper values of surface resistance are always important. We should also use modes with negligible $P^{\|}_{samp}$ because we obtained equation (3.18) by neglecting $P^{\|}_{samp}tan\delta_\|$ term in (3.17). We can see from table 4.2 to table 4.7 that all of these modes meet the demand.

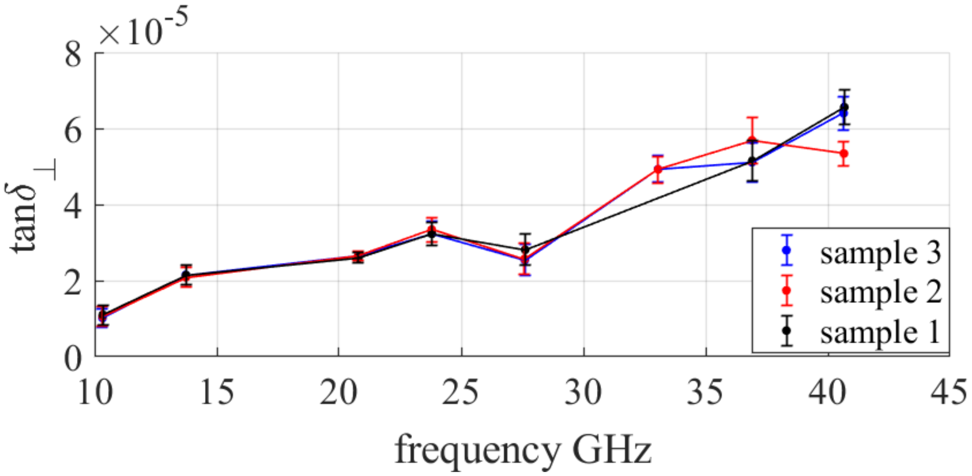

Figure 4.6: perpendicular components of loss tangent versus frequency for the 12 mm samples at room temperature

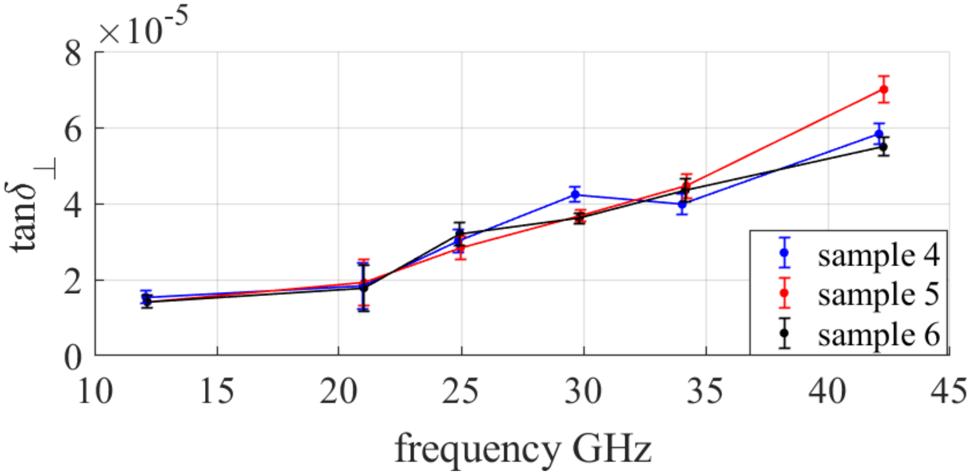

Figure 4.7: perpendicular components of loss tangent versus frequency for the 8 mm samples at room temperature.

f(GHz)	Q	$\epsilon_\perp$	$tan\delta_\perp(\times10^{-5})$	G	$P^{\perp}_{samp}$	$P^{\parallel}_{samp}$	m	PDR
10.3234	31512.7	9.372	1.02	1460	0.887	0	0	0
13.7310	26519.9	9.367	2.15	1886	0.817	0.001	1	0.55
20.7840	28356.1	9.358	2.65	3473	0.814	0.001	1	2.49
23.7949	20381.8	9.337	3.24	1695	0.601	0	0	0
27.6018	18835.1	9.405	2.54	1367	0.556	0	0	11.30
33.0507	20689.0	9.361	4.93	6218	0.754	0.037	5	48.97
36.8985	18583.7	9.380	5.11	4661	0.786	0.008	3	6.77
40.6418	15538.0	9.378	6.40	7717	0.868	0.004	2	18.76

Table 4.2: Detailed data of sample 3.

f(GHz)	Q	$\epsilon_\perp$	$tan\delta_\perp(\times10^{-5})$	G	$P^{\perp}_{samp}$	$P^{\parallel}_{samp}$	m
10.3269	31159.8	9.373	1.06	1443	0.887	0	0
13.7339	26865.1	9.371	2.09	1886	0.811	0.001	1
20.7857	28386.8	9.364	2.65	3471	0.814	0.001	1
23.7918	20115.2	9.347	3.34	1694	0.600	0	0
27.5943	18764.7	9.417	2.57	1366	0.555	0	0
33.0573	20714.4	9.365	4.92	6249	0.754	0.037	5
36.8931	17124.3	9.390	5.69	4661	0.786	0.008	3
40.6556	18137.3	9.377	5.34	7687	0.878	0.004	2

Table 4.3: Detailed data of sample 2.

f(GHz)	Q	$\epsilon_\perp$	$tan\delta_\perp(\times10^{-5})$	G	$P^{\perp}_{samp}$	$P^{\parallel}_{samp}$	m
10.3358	30861.3	9.366	1.10	1443	0.887	0	0
13.7438	26556.9	9.362	2.14	1886	0.811	0.001	1
20.7963	28706.5	9.356	2.60	3464	0.813	0.001	1
23.7941	20401.8	9.347	3.23	1693	0.600	0	0
27.6153	18351.7	9.394	2.81	1372	0.557	0	0
36.9027	18477.9	9.383	5.15	4670	0.796	0.008	3
40.6701	15189.7	9.371	6.56	7598	0.877	0.005	2

Table 4.4: Detailed data of sample 1.

f(GHz)	Q	$\epsilon_\perp$	$tan\delta_\perp(\times 10^{-5})$	G	$P^{\perp}_{samp}$	$P^{\parallel}_{samp}$	m	PDR
12.0941	33955.0	9.364	1.54	2194	0.857	0	0	0
20.9781	20777.9	9.412	1.82	1153	0.432	0	0	0
24.8808	20732.9	9.369	3.01	1719	0.612	0	0	0
29.6649	25692.5	9.375	4.24	29232	0.833	0.046	4	2.74
34.0416	23225.3	9.382	3.98	4325	0.737	0	0	0
42.0940	18022.1	9.390	5.83	5422	0.721	0.023	4	13.33

Table 4.5: Detailed data of sample 4.

f(GHz)	Q	$\epsilon_\perp$	$tan\delta_\perp(\times 10^{-5})$	G	$P^{\perp}_{samp}$	$P^{\parallel}_{samp}$	m
12.1634	35287.2	9.362	1.42	2219	0.855	0	0
20.0287	20148.1	9.418	1.91	1113	0.413	0	0
24.9723	21684.8	9.362	2.84	1814	0.630	0	0
29.8855	29202.4	9.377	3.68	28710	0.832	0.046	4
34.2103	21376.9	9.382	4.46	4002	0.715	0	0
42.2923	15571.2	9.389	7.00	5414	0.720	0.023	4

Table 4.6: Detailed data of sample 5.

f(GHz)	Q	$\epsilon_\perp$	$tan\delta_\perp(\times 10^{-5})$	G	$P^{\perp}_{samp}$	$P^{\parallel}_{samp}$	m
12.1485	35272.5	9.369	1.42	2208	0.855	0	0
20.0150	20504.7	9.421	1.78	1125	0.419	0	0
24.9434	21373.4	9.369	3.21	1781	0.624	0	0
29.8166	29752.1	9.383	3.61	29209	0.836	0.043	4
34.1593	21820.9	9.387	4.34	4136	0.724	0	0
42.2645	18865.9	9.396	5.49	5325	0.721	0.018	4

Table 4.7: Detailed data of sample 6.

Detailed information about the error bars is presented from table 4.8 to table 4.13. We calculate these errors with equation (3.19). For $\epsilon_\perp$, (3.19) should be expanded as:

$$\begin{aligned}\sigma_{\epsilon_\perp} = [(\frac{\partial\epsilon_\perp}{\partial D_{res}}\sigma_{D_{res}})^2 + (\frac{\partial\epsilon_\perp}{\partial H_{res}}\sigma_{H_{res}})^2 + (\frac{\partial\epsilon_\perp}{\partial D_{samp}}\sigma_{D_{samp}})^2 \\ +(\frac{\partial\epsilon_\perp}{\partial H_{samp}}\sigma_{H_{samp}})^2 + (\frac{\partial\epsilon_\perp}{\partial f}\sigma_f)^2]^{\frac{1}{2}}\end{aligned} \tag{4.4}$$

Where $\sigma_{H_{res}}$ and $\sigma_{D_{Res}}$ are one standard deviation of the height and the diameter of the resonator and $\sigma_{H_{samp}}$ and $\sigma_{D_{samp}}$ are one standard deviation of the height and the diameter of the sample. These four values have been presented in table 4.1. σ_f is the uncertainty of the resonant frequency. We measure ten times for each resonant mode to get 10 values of resonant frequency f and again use (3.20) and (3.21) to calculate σ_f. We can also get the uncertainty of the unloaded quality factor σ_Q in this way, which we need in the calculation for the $\sigma_{tan\delta_\perp}$. In addition, after each measurement, we take out the sample, put it in and center it again to start the next measurement. Therefore besides the systematic error, σ_f and σ_Q are also caused by the potential deviation of the sample from the center. Finally, all partial derivatives in (4.4) can be obtained in COMSOL as already mentioned in section 3.3. For $\sigma_{tan\delta_\perp}$, we use:

$$\sigma_{tan\delta_\perp} = \sqrt{(\frac{\partial tan\delta_\perp}{\partial Q}\sigma_Q)^2 + (\frac{\partial tan\delta_\perp}{\partial R_s}\sigma_{R_s})^2} \tag{4.5}$$

The partial derivatives can be calculated using equations (3.22) and (3.23). The uncertainty of surface resistance σ_{R_s} is obtained as 3 mΩ as explained in section 4.2. Since σ_f, σ_Q and partial derivatives are the same, so these values are not presented in all of the tables. The largest error of $\epsilon_\perp$ is 0.0071,about 0.076% of the corresponding measured value. For most of modes, the error in $\epsilon_\perp$ is mainly caused by the uncertainty of dimensions of the sample. For 8 mm group, the effect of uncertainty of the diameter is quite dominant since 8 mm samples have larger uncertainties in diameter compared to 12 mm ones. When $\partial\epsilon_\perp/\partial D_{samp}$ is larger, the resonance frequencies are more sensitive to the diameter. The uncertainty in f and dimensions of the resonator generally have a smaller effect on final results. The relative errors in $tan\delta_\perp$ are larger. For modes with low G (<3000), the uncertainty is mainly caused by R_s otherwise the uncertainty in Q contributes to $\sigma_{tan\delta_\perp}$. We see a large error bar at 21 GHz caused by the very low G (only 1100). Additionally, dimensions of resonator and the samples and $\epsilon_\perp$ also add to the uncertainty to $tan\delta_\perp$ but they can be safely neglected compared with Q and R_s. Finally, the coupling coefficients also has an impact on the resonant frequency. We always control our $S_{11,0}$ and $S_{22,0}$ below 0.3 dB. In this range, we have seen how much the resonant frequency and the quality factor change for the 10 and 21 GHz modes, one with high $P^\perp_{samp}$ and the other with low $P^\perp_{samp}$. We find that changes for f for both modes are less than 0.1 MHz and for Q are about 200. Thus an assumption is made that we can safely neglect these effects.

f(GHz)	$\sigma_{\epsilon_\perp}(10^{-3})$	$\sigma_{tan\delta_\perp}$	$\sigma_{H_{res}}\lvert\frac{\partial\epsilon}{\partial H_{res}}\rvert$	$\sigma_{D_{res}}\lvert\frac{\partial\epsilon}{\partial D_{res}}\rvert$	$\sigma_{H_{samp}}\lvert\frac{\partial\epsilon}{\partial H_{samp}}\rvert$	$\sigma_{D_{samp}}\lvert\frac{\partial\epsilon}{\partial D_{samp}}\rvert$	$\sigma_f\lvert\frac{\partial\epsilon}{\partial f(GHz)}\rvert$	$\sigma_f(MHz)$	σ_Q
10.3234	2.55	0.25×10^{-5}	0.60×10^{-3}	0.07×10^{-3}	1.93×10^{-3}	1.37×10^{-3}	1.03×10^{-3}	0.37	858
13.7310	2.72	0.26×10^{-5}	0.45×10^{-3}	0.11×10^{-3}	1.66×10^{-3}	1.80×10^{-3}	0.84×10^{-3}	0.66	974
20.7840	2.48	0.13×10^{-5}	0.41×10^{-3}	0.13×10^{-3}	1.13×10^{-3}	1.88×10^{-3}	0.56×10^{-3}	0.96	485
23.7949	3.68	0.31×10^{-5}	1.54×10^{-3}	0.50×10^{-3}	0.92×10^{-3}	1.41×10^{-3}	0.76×10^{-3}	1.84	232
27.6018	4.29	0.40×10^{-5}	2.46×10^{-3}	0.81×10^{-3}	0.58×10^{-3}	0.70×10^{-3}	0.62×10^{-3}	2.59	169
33.0507	2.79	0.35×10^{-5}	0.42×10^{-3}	0.25×10^{-3}	0.65×10^{-3}	1.91×10^{-3}	0.33×10^{-3}	5.30	1400
36.8985	4.02	0.52×10^{-5}	0.13×10^{-3}	0.10×10^{-3}	1.47×10^{-3}	2.22×10^{-3}	0.38×10^{-3}	1.12	1276
40.6418	2.78	0.44×10^{-5}	0.05×10^{-3}	0.13×10^{-3}	0.74×10^{-3}	1.95×10^{-3}	0.27×10^{-3}	3.43	926

Table 4.8: Detailed data of errors of sample 3

f(GHz)	$\sigma_{\epsilon_\perp}(10^{-3})$	$\sigma_{tan\delta_\perp}$	$\sigma_{H_{samp}}\lvert\frac{\partial\epsilon}{\partial H_{samp}}\rvert$	$\sigma_{D_{samp}}\lvert\frac{\partial\epsilon}{\partial D_{samp}}\rvert$
10.3269	1.64	0.25×10^{-5}	0.97×10^{-3}	0.91×10^{-3}
13.7339	1.89	0.26×10^{-5}	0.83×10^{-3}	1.2×10^{-3}
20.7857	1.80	0.13×10^{-5}	0.57×10^{-3}	1.26×10^{-3}
23.7918	3.44	0.31×10^{-5}	0.46×10^{-3}	0.94×10^{-3}
27.5943	4.23	0.40×10^{-5}	0.29×10^{-3}	0.47×10^{-3}
33.0573	1.86	0.35×10^{-5}	0.33×10^{-3}	1.27×10^{-3}
36.8931	3.72	0.61×10^{-5}	0.74×10^{-3}	1.48×10^{-3}
40.6556	2.97	0.33×10^{-5}	0.37×10^{-3}	1.30×10^{-3}

Table 4.9: Detailed data of errors of sample 2

f(GHz)	$\sigma_{\epsilon_\perp}(10^{-3})$	$\sigma_{tan\delta_\perp}$	$\sigma_{H_{samp}}\lvert\frac{\partial\epsilon}{\partial H_{samp}}\rvert$	$\sigma_{D_{samp}}\lvert\frac{\partial\epsilon}{\partial D_{samp}}\rvert$
10.3358	3.19	0.26×10^{-5}	2.89×10^{-3}	0.91×10^{-3}
13.7438	3.01	0.26×10^{-5}	2.49×10^{-3}	1.20×10^{-3}
20.7963	2.41	0.13×10^{-5}	1.70×10^{-3}	1.26×10^{-3}
23.7941	3.67	0.31×10^{-5}	1.37×10^{-3}	0.94×10^{-3}
27.6153	4.31	0.40×10^{-5}	0.87×10^{-3}	0.47×10^{-3}
36.9027	3.83	0.52×10^{-5}	2.21×10^{-3}	1.48×10^{-3}
40.6701	3.15	0.46×10^{-5}	1.11×10^{-3}	1.30×10^{-3}

Table 4.10: Detailed data of errors of sample 1

f(GHz)	$\sigma_{\epsilon_\perp}(10^{-3})$	$\sigma_{tan\delta_\perp}$	$\sigma_{H_{res}}\lvert\frac{\partial\epsilon}{\partial H_{res}}\rvert$	$\sigma_{D_{res}}\lvert\frac{\partial\epsilon}{\partial D_{res}}\rvert$	$\sigma_{H_{samp}}\lvert\frac{\partial\epsilon}{\partial H_{samp}}\rvert$	$\sigma_{D_{samp}}\lvert\frac{\partial\epsilon}{\partial D_{samp}}\rvert$	$\sigma_f\lvert\frac{\partial\epsilon}{\partial f(GHz)}\rvert$	$\sigma_f(MHz)$	σ_Q
12.0941	4.46	0.17×10^{-5}	0.65×10^{-3}	0.05×10^{-3}	1.08×10^{-3}	4.26×10^{-3}	0.46×10^{-3}	0.25	621
20.9781	5.05	0.61×10^{-5}	2.64×10^{-3}	0.78×10^{-3}	0.64×10^{-3}	4.02×10^{-3}	0.94×10^{-3}	0.46	123.8
24.8808	4.18	0.30×10^{-5}	1.17×10^{-3}	0.54×10^{-3}	0.49×10^{-3}	3.59×10^{-3}	1.53×10^{-3}	1.25	270.4
29.6649	6.00	0.20×10^{-5}	0.01×10^{-3}	0.02×10^{-3}	0.35×10^{-3}	5.09×10^{-3}	0.56×10^{-3}	0.74	1143
34.0416	4.64	0.27×10^{-5}	0.30×10^{-3}	0.31×10^{-3}	0.53×10^{-3}	4.55×10^{-3}	0.44×10^{-3}	0.59	1003
42.0940	5.80	0.26×10^{-5}	0.25×10^{-3}	0.23×10^{-3}	1.49×10^{-3}	5.50×10^{-3}	0.75×10^{-3}	1.21	607

Table 4.11: Detailed data of sample 4.

f(GHz)	$\sigma_{\epsilon_\perp}(10^{-3})$	$\sigma_{tan\delta_\perp}$	$\sigma_{H_{samp}}\lvert\frac{\partial\epsilon}{\partial H_{samp}}\rvert$	$\sigma_{D_{samp}}\lvert\frac{\partial\epsilon}{\partial D_{samp}}\rvert$
12.1634	5.20	0.17×10^{-5}	0.54×10^{-3}	5.10×10^{-3}
21.0287	5.70	0.61×10^{-5}	0.32×10^{-3}	4.82×10^{-3}
24.9723	4.80	0.30×10^{-5}	0.25×10^{-3}	4.31×10^{-3}
29.8855	7.10	0.15×10^{-5}	0.18×10^{-3}	7.10×10^{-3}
34.2103	5.50	0.31×10^{-5}	0.27×10^{-3}	5.50×10^{-3}
42.2923	6.70	0.34×10^{-5}	0.75×10^{-3}	6.60×10^{-3}

Table 4.12: Detailed data of errors of sample 5

f(GHz)	$\sigma_{\epsilon_\perp}(10^{-3})$	$\sigma_{tan\delta_\perp}$	$\sigma_{H_{samp}}\lvert\frac{\partial\epsilon}{\partial H_{samp}}\rvert$	$\sigma_{D_{samp}}\lvert\frac{\partial\epsilon}{\partial D_{samp}}\rvert$
12.1485	4.36	0.17×10^{-5}	0.54×10^{-3}	4.26×10^{-3}
21.0150	5.05	0.61×10^{-5}	0.32×10^{-3}	4.02×10^{-3}
24.9434	4.16	0.30×10^{-5}	0.25×10^{-3}	3.59×10^{-3}
29.8166	6.00	0.15×10^{-5}	0.18×10^{-3}	5.09×10^{-3}
34.1593	4.61	0.30×10^{-5}	0.27×10^{-3}	4.55×10^{-3}
42.2645	5.60	0.24×10^{-5}	0.75×10^{-3}	5.50×10^{-3}

Table 4.13: Detailed data of errors of sample 6

Figure 4.8 shows a comparison of different results of $\epsilon_\perp$ measurement at room temperatures from other works. Here we choose only sample 3 and sample 6 to present in this and following several plots so that plots are simple and neat. Breeze[13], Krupka[15][10], Egorov[20] and Kobayashi[21] give 9.39-9.40 around 10 GHz, which are different from this work. Krupka also gives one around 22 GHz. Ebata[12] also provides three more data distributed from 32 GHz to 44 GHz, whose trend is similar to those of sample 6, but the values are all smaller. In the work by Karpisz[22], $\epsilon_\perp$ is obtained as a constant of 9.401 in the frequency range 20-50 GHz with an uncertainty of ±0.1. This error bar value exceeds the range of our plot so it is not presented. In addition, we made a fit of form $af^b + c$ for sample 6 after deleting points at 21 and 25 GHz, where we have $b = 1.531$, $c = 9.364$ and $a \approx 10^{-4}$. The small value of 'a' indicates the weak dependence on frequency. Indeed, if we look at data from Breeze, Krupka, Egorov, Kobayashi and Karpisz, we can see over the frequency span, no obvious dependence on frequency is shown.

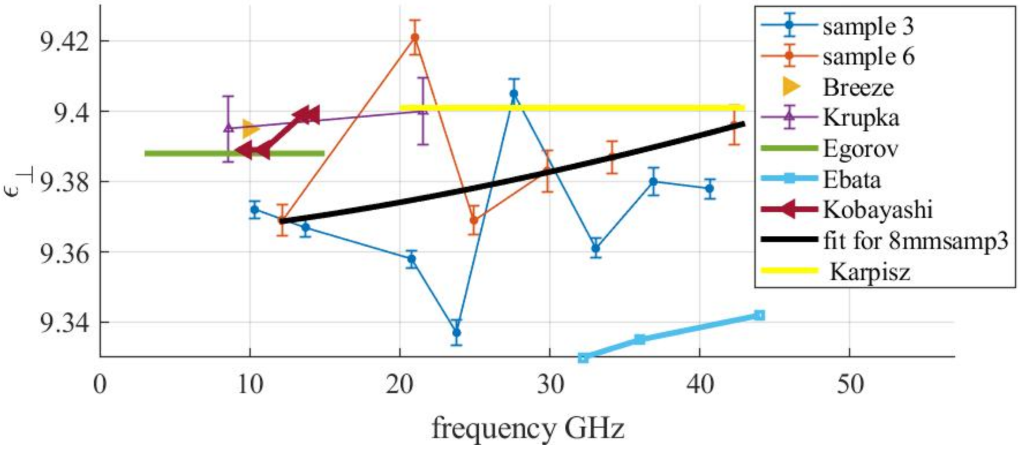

Figure 4.8: A comparison of our results of $\epsilon_\perp$ at room temperatures with that cited from other literature

Figure 4.9 shows a comparison of different results $tan\delta_\perp$ measurement at room temperatures from other works. In addition, a fit for both samples of form $af^b + c$ is made and we get b=1.382, which is different from the power of 0.84 given by Hartnett in frequency range from 7 GHz to 16 GHz. Breeze gives 5×10^{-6} at 10 GHz, which is a little bit lower than that of this work. Krupka's result fits the results of sample 6 of this work. Finally, $tan\delta_\perp$ is measured to be around 3.5×10^{-5} in the range 32-44 GHz in Ebata's work, which is also lower than those of this work. In the work by Karpisz, $tan\delta_\perp$ is almost linearly dependent on the frequency as shown in figure 4.10. We can learn that $tan\delta_\perp$ has an obvious increasing trend with the frequency. Our results, a combination of results of cited literature in figure 4.9 and results from Karpisz in figure 4.10 can all be good evidences for it.

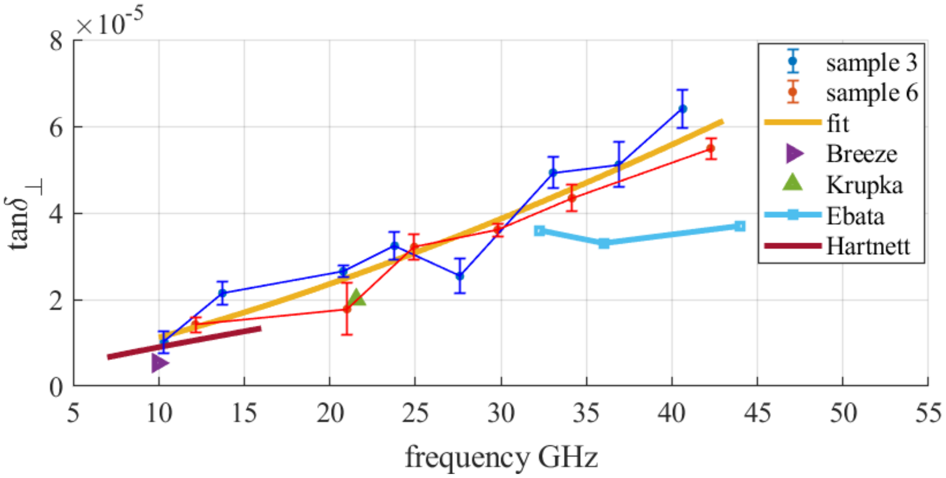

Figure 4.9: A comparison of our results of $tan\delta_{\perp}$ at room temperature with that cited from other literature

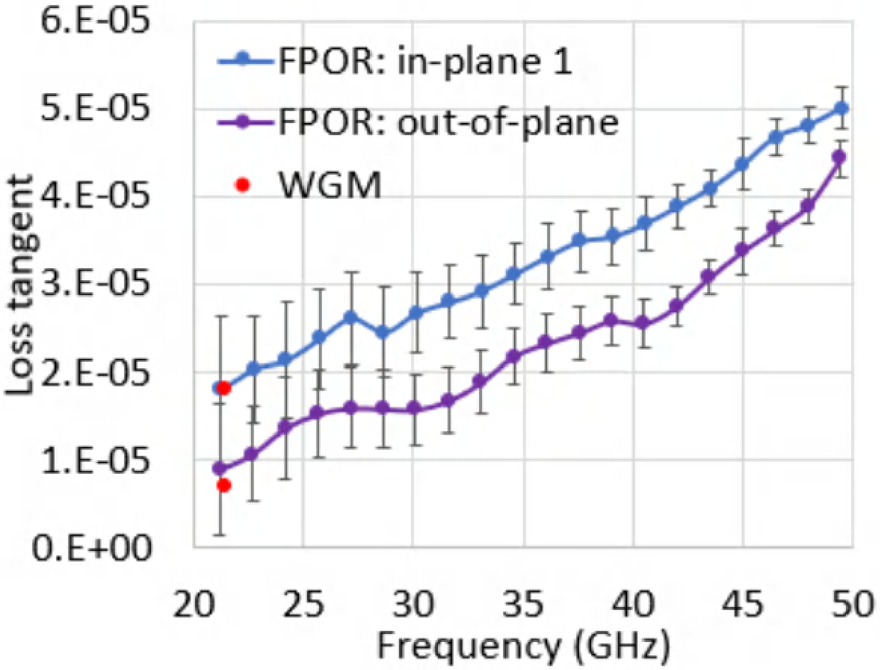

Figure 4.10: $tan\delta_{\perp}$ (in-plane 1) and $tan\delta_{\parallel}$ (out-of-plane) of the sapphire as a function of frequency at room temperature[22].

4.4 Results of mode identification

Figure 4.11 compares the changes in resonance frequencies of VNA and COMSOL when shifting the sample by 0.5 mm away from the center. The x axis shows mode names and for a certain mode there are two values. One is for VNA and another for COMSOL. The two changes for almost all of the modes are close enough except the 17.35 GHz one, which has an opposite behaviour and thus the 17.35 GHz mode is not adapted in the $\epsilon_\perp$ or $tan\delta_\perp$ plots and tables. This diagram proves that we do match a proper mode in COMSOL with what we obtain with VNA. In case that changes for some modes are not close when the sample is shifted 1 mm away from the center, some tests on 1 mm shift have also been done for five modes and the results are shown in figure A.1. In addition, PTFE removal experiment is also conducted for five modes and the results are presented in figure A.2.

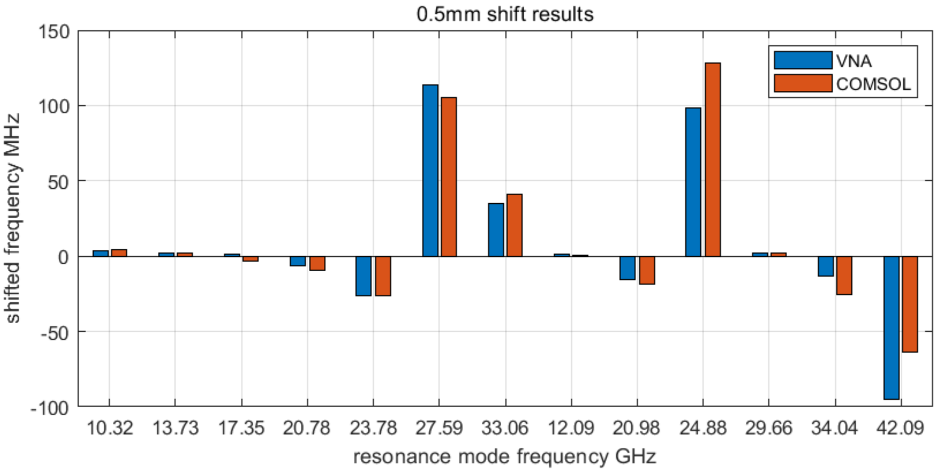

Figure 4.11: Comparison of difference in f when the sample is shifted 0.5 mm away from the center for different modes

An example of choosing the proper mode is shown here: A resonance mode around 20.9 GHz has been found with VNA. The difference of frequencies Δf_{vna} with the sample shifted by 0.5 mm and with the sample centered is 15.24 MHz. There are two candidate modes found in COMSOL with m=0 and m=3 (figure 4.12). For m=0 mode, the difference of frequencies Δf_{comsol} with the sample shifted by 0.5 mm and with the sample centered is -18 MHz while for m=3 mode, It is -36 MHz. Since Δf_{comsol} of m=0 mode is more close to Δf_{vna}, m=0 one is chosen.

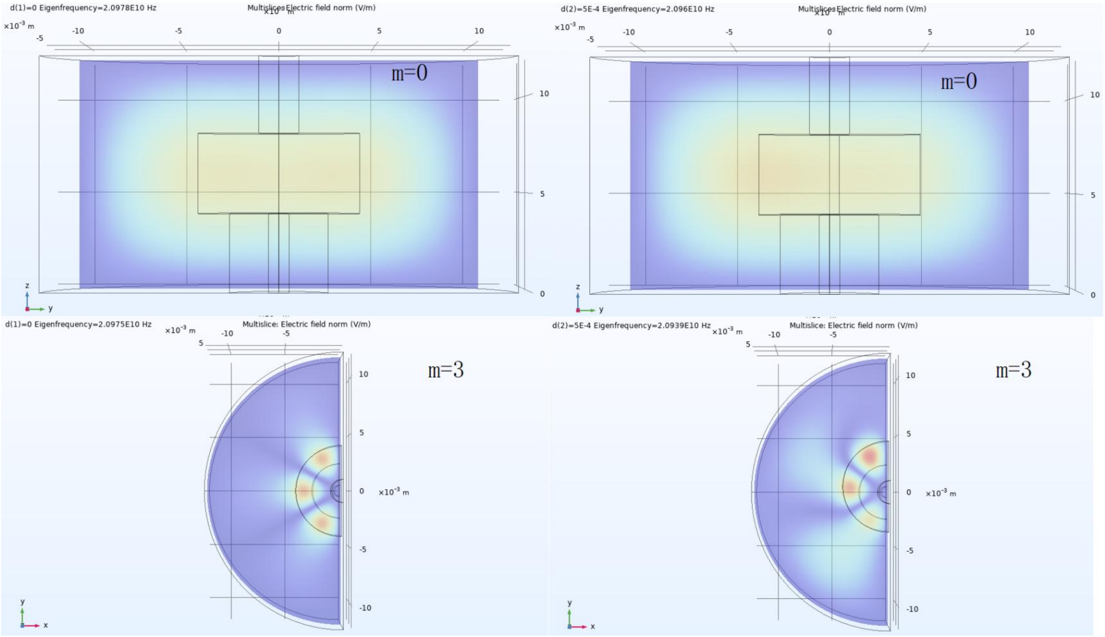

Figure 4.12: Two modes of m=0 and m=3 found on COMSOL for one resonance mode on VNA. The sample in the first column is centered while in the second column it is shifted by 0.5 mm from the center

In addition, even though we find only one appropriate mode in COMSOL simulation, it can also be suspicious because of its deviation from the overall trend and needs to be tested. The deleted 17.35 GHz mode is an example of this. Thus though there are modes with only one correspondence in COMSOL, it is still meaningful to test it with the mode identification method.

4.5 The results of cryogenic experiment

Figure 4.13 shows $\epsilon_\perp$ of sample 3 in the cryogenic experiment around 18 K together with data from other two works. Detailed data are shown in table 4.14. Remember we should use modes with high P_{samp} and negligible $P^{||}_{samp}$ so the data of sample 3 are divided into two parts: those with P_{samp}>0.7 and negligible $P^{||}_{samp}$ (blue) and the others (black) with $P_{samp} < 0.7$ or non-negligible $P^{||}_{samp}$, for which we give low credence. The $\epsilon_\perp$ is lower at this temperature. It also has a decrease trend between 10 GHz and 21 GHz. After that there is a peak at 27.8 GHz. If we only look at blue ones, $\epsilon_\perp$ is almost constant. The error bar at the end is caused by the lack of ability to identify modes on COMSOL. Around 32.7 GHz, two modes are found on VNA but only one appropriate mode is found on COMSOL so we match those two on VNA with the same one on COMSOL. They are close enough to each other so it looks like only one point is there. Since in the cryogenic experiment it is not possible to do the sample shift or remove the PTFE rod, mode identification test has not been done. The value at around 10 GHz is near to that in Breeze's work. The difference is less than 0.01 while there is a difference between this work and Krupka's. Since at room temperature we see the error bars are mostly caused by uncertainties of dimension and the ratio of dimensions of both resonator and samples at 18 K to that at room temperature is very close to 1. Together with that the uncertainties of dimensions are proportional to the dimension, thus we use the same error bars here for modes which we also found in room temperature experiment. For those newly discovered mode at 18 K, we give it the largest error bar among those we have at room temperature as an approximation. We can learn from the figure that if we only look at the blue points, $\epsilon_\perp$ still shows no obvious dependence on frequency.

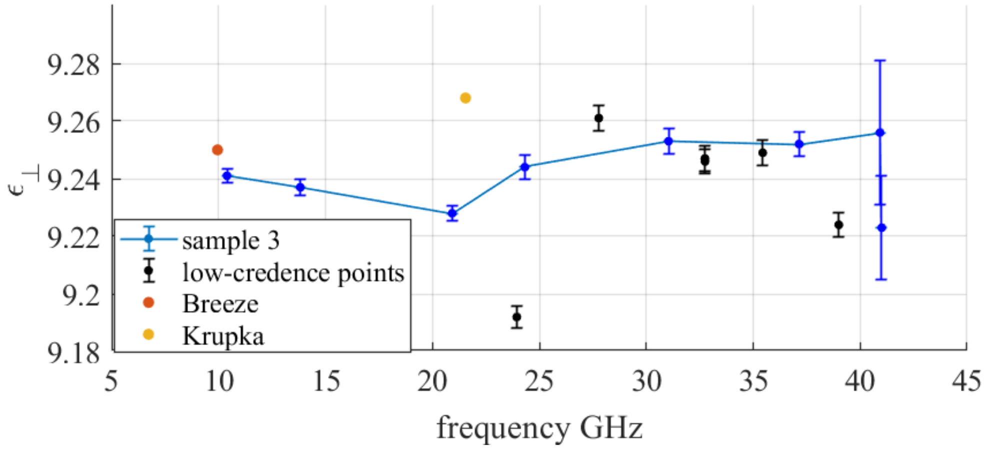

Figure 4.13: Perpendicular components of dielectric constant versus frequency of sample 3 at 18 K

Figure 4.14 shows the results of $tan\delta_\perp$ of sample 3 in the cryogenic experiment around 18 K. The information about parameters in equation (3.18) at 18 K is provided by E. Öz[19]. Detailed data are shown in table 4.14. The values of $tan\delta_\perp$ are generally smaller but the pattern looks quite different here. There is not an increasing trend over the entire frequency range. Most of the points have a value about 10^{-6}. There is also a dramatic peak around 24 GHz. In work by Breeze[13], a value of $tan\delta_\perp$ at the same temperature is given as 10^{-8} at 10 GHz while Krupka [10] gives 3.5×10^{-8} at 21.55 GHz. Since at 18 K, it is impossible to take the sample out and put it back to do multiple measurements as we do at room temperature, we only consider the uncertainty caused by the surface resistance, which is assumed to be 3 mΩ as used at room temperature. Then $\sigma_{tan\delta_\perp}$ is calculated by

$$\sigma_{tan\delta_\perp} = \sqrt{(\frac{\partial tan\delta_\perp}{\partial R_s}\sigma_{R_s})^2} \tag{4.6}$$

A majority of $P^\perp_{samp}$ is larger than 0.7. For 32 and 35 and 39 GHz, $P^{||}_{samp}$ can not be neglected so these modes should not be included, but they fit well in the plots and anyway are kept there and given low credence. In addition, there are G factors more than a hundred thousand or even a few millions, which are more reliable for getting $tan\delta_\perp$ compared with those of a few thousands. We can see each of the last two modes is matched with two modes found in COMSOL, which contributes dominantly to the error bars of the 40.93 and 41.01 GHz modes.

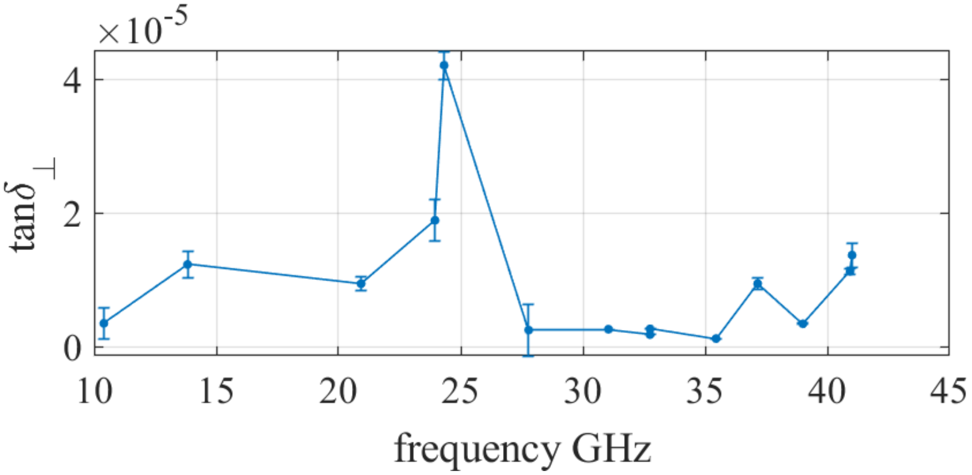

Figure 4.14: Perpendicular components of loss tangent versus frequency of sample 3 in cryogenic experiment

f(GHz)	Q	$\epsilon_{\perp}$	$tan\delta_{\perp}(\times 10^{-6})$	G	$P^{\perp}_{samp}$	$P^{\parallel}_{samp}$	m
10.3978	71481.5	9.241	3.49	1439	0.886	0	0
13.8229	50480.5	9.237	12.3	1904	0.812	0.001	1
20.9239	69157.8	9.228	9.42	3410	0.810	7e-4	1
23.9456	38025.1	9.192	18.9	1660	0.592	0	0
24.3199	23620.2	9.244	42.1	1998	0.720	6e-4	2
27.7786	49376.5	9.261	2.48	1393	0.563	0	0
31.0445	396995	9.253	2.61	729747	0.947	0.003	7
32.7444	517748	9.247	1.80	134051	0.267	0.685	6
32.7448	363874	9.246	2.66	134166	0.267	0.685	6
35.4438	829682	9.249	1.21	810499	0.246	0.719	7
37.1464	71824.2	9.252	9.43	4766	0.797	0.008	3
39.0020	255919	9.224	3.43	36013	0.669	0.219	7
40.9300	88669.8	9.281	11.7	4108088	0.891	0.070	8
40.9300	88669.8	9.231	10.8	18967	0.809	0.075	2
41.0103	66934.1	9.241	15.5	4234504	0.891	0.069	8
41.0103	66934.1	9.205	11.9	7213	0.856	0.009	5

Table 4.14: Detailed data of sample 3 in cryogenic experiment.

5 Further Discussions

In this chapter, Relevant theories about dielectric properties are discussed from literature. In addition, we evaluate the loss tangent for modes with high geometric factor in order to mitigate the uncertainty caused by surface resistance. We also evaluate $\epsilon_\perp$ for modes with high $P^\perp_{samp}$.

5.1 Theoretical models for dielectric properties

Figure 5.1 shows a rough relation between real and imaginary parts of dielectric constant and the frequency. We see the main contribution to the permittivity changes with the frequency. At frequencies around and below microwave range, the dipolar polarization is dominant, which is caused by the same orientation of molecules with dipoles. As the frequency goes up, the Electromagnetic field alternates faster and there is not enough time for those molecules to be arranged in the same direction so contribution due to this goes down. Around 10^{12} Hz, the atom or ionic polarization is prominent, which result from the displacement of ions. Then around 10^{15} Hz, the electronic polarization becomes important.

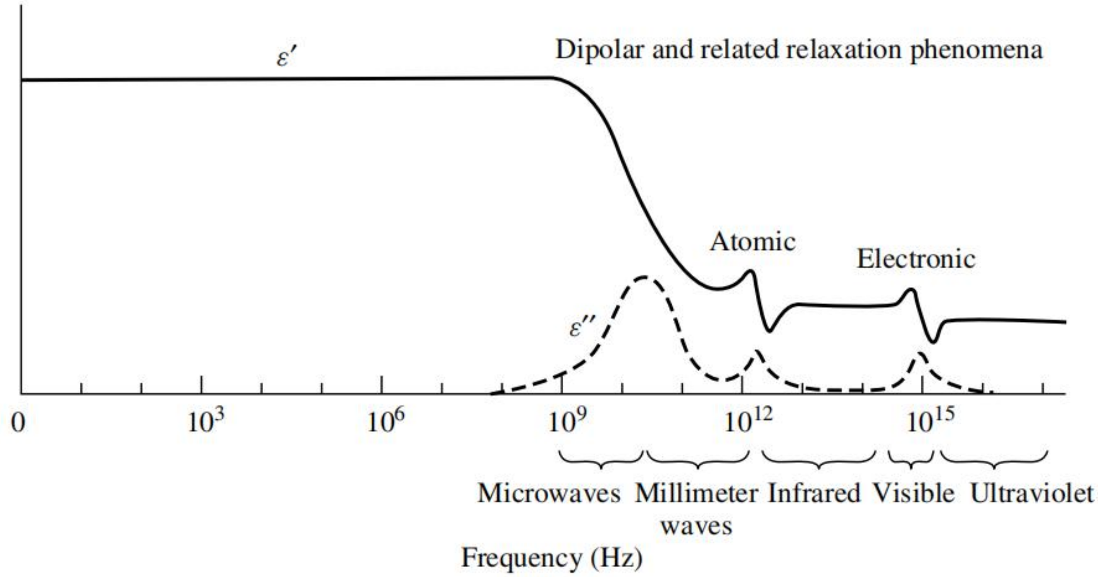

Figure 5.1: Dielectric dispersion for various types of polarization[23]

There is a simple model for dielectric properties, in which the crystal is composed of classical resonators of different natural frequencies with damping[24]:

$$\epsilon(\omega) = \epsilon_\infty + \sum_{j}^{N} \frac{S_j \omega_j}{\omega_j^2 - \omega^2 - i\omega\Gamma_j} \tag{5.1}$$

The first term stands for the dielectric constant when frequency goes to infinity, which is determined by electronic polarizability and the second term represents the lattice as N classical harmonic oscillators with eigenfrequency ω_j, damping factor Γ_j and oscillator strength S_j.

If the microwave frequency ω is much smaller than natural frequencies of those oscillators, then ϵ_r and $tan\delta$ can be written as[25]:

$$\epsilon_r = \frac{1}{\epsilon_0}(\epsilon_\infty + \sum_{j=1}^{N} S_j) \tag{5.2}$$

$$tan\delta = \frac{\omega}{\epsilon_0 \epsilon_r} \sum_{j=1}^{N} \frac{S_j \Gamma_j}{\omega_j^2} \tag{5.3}$$

which shows that dielectric constant has no strong dependence on frequency and loss tangent is linearly dependent on frequency.

In both works by Braginsky [26] and Zuccaro[27], the dielectric loss is composed of two parts. One is the intrinsic loss caused by the interaction between an electromagnetic field and the phonon system of the dielectric. The other is the loss caused by imperfections of the dielectric. The fundamental loss tangent formulas for hexagonal and cubic (rhombohedric) crystals are given by Gurevich respectively as[28]

$$tan\delta \approx \eta \frac{\omega(kT)^5}{\epsilon\rho v^5 \hbar^2 (kT_D)^2} \tag{5.4}$$

$$tan\delta \approx \eta \frac{\omega^2(kT)^4}{\epsilon\rho v^5 \hbar (kT_D)^2} \tag{5.5}$$

where k is Boltzmann constant, ϵ is the permittivity, $\hbar$ is the reduced Planck constant, ρ is the density and v the mean sound speed. η is a dimensionless parameter in the range to 10-100. These two equations are effective when temperature is much smaller than the Debye temperature (T_D). For sapphire, T_D=1047 K[29].

Another way to describe the microwave absorption due to the interaction between phonons and electromagnetic waves is the model developed by Sparks, King and Mills[30], which is based on lifetime broadened two phonon difference processes. In this model, loss tangent is given by:

$$tan\delta \propto \phi_3^2 \frac{hf}{k_B T} n(\nu_1)[n(\nu_1)+1][tan^{-1}(\nu_{TO}/\gamma) - tan^{-1}(\Delta\nu/\gamma)] \tag{5.6}$$

where ϕ_3 is the third derivative of the lattice potential, ν_{TO} is the frequency of the fundamental reststrahlen mode, ν_1 is the frequency of the phonon, $\Delta\nu$ is the change of the frequency of the phonon after the interaction and n is the Bose function:

$$n(\nu_1) = \frac{1}{e^{(\frac{h\nu_1}{k_B T})} - 1} \tag{5.7}$$

where k_B is Boltzmann constant. According to equation (5.6), the loss tangent caused by interaction between electromagnetic wave and phonons is linearly dependent on the frequency.

For the loss caused by defect dipole relaxations, Zuccaro[27] uses the Debye formula

$$\epsilon' - j\epsilon'' = \epsilon_\infty + \frac{\epsilon_s - \epsilon_\infty}{1+\omega^2\tau^2} - j\frac{(\epsilon_s - \epsilon_\infty)\omega\tau}{1+\omega^2\tau^2} \tag{5.8}$$

where ϵ_s is the permittivity when the frequency of electromagnetic wave is 0 and ϵ_∞ is the permittivity when the frequency goes to infinity. τ is the dipole relaxation time, which is the time dipoles need to return to the equilibrium. If the defect dipoles have different relaxation time, generally we have[31]

$$\epsilon' - j\epsilon'' = \epsilon_\infty + (\epsilon_s - \epsilon_\infty)\int\limits_{s}^{\infty} \frac{D(\tau)(1-j\omega\tau)}{1+\omega^2\tau^2}d\tau \tag{5.9}$$

where

$$\int\limits_{0}^{\infty} D(\tau)d\tau = 1 \tag{5.10}$$

The Cole-Cole distribution is one of the most common one and reduces (5.9) to

$$\epsilon' - j\epsilon'' = \epsilon_\infty + \frac{\epsilon_0 - \epsilon_\infty}{1+(j\omega\tau)^{1-m}} \tag{5.11}$$

where 0⩽m⩽1. Then the loss tangent caused by defect dipoles is:

$$tan\delta = \frac{\theta(\omega\tau)^{1-m}sin[(1-m)\frac{pi}{2}]}{1+\theta+(2+\theta)(\omega\tau)^{1-m}cos[(1-m)\frac{pi}{2}]+(\omega\tau)^{2(1-m)}} \tag{5.12}$$

where θ=$(\epsilon_s - \epsilon_\infty)/\epsilon_\infty$.

5.2 Further discussions on results

We notice that the error bars of $tan\delta_\perp$ are proportional to $\frac{1}{G}$. Those with a small G have a much larger error bar compared with those with a much larger G. If we want to reduce the effect of R_s, choosing modes with a large G is a sensible way.

We choose modes with G bigger than 3000 and make new plots at room temperature. Figure 5.2 shows the results of modes with G bigger than 3000 of both sample 3 and sample 6, in which a fit of form $af^b + c$ is made and b is equal to 1.112. Thus the fit is close to a linear dependence on frequency as shown in equation (5.3), (5.4) and (5.6). Relative parameters in equation (5.4) are given for sapphire at 300 K[29]: ρ=4000 kg/m^3, v=6000 m/s, $\eta = 100$ and T_D=1047 K. With these values, a plot of equation (5.4) is made. In addition, Braginsky shows that in temperature range 60-150 K, $tan\delta$ is linearly dependent on f^β, where $\beta \approx 1.7$, contrary to equation (5.4) and (5.5). The reason for it is that sapphire is not in the hexagonal symmetry class and its lattice is of rhombohedric symmetry. However, its acoustic spectrum is similar to that of a hexagonal crystal. Therefore β is obtained between 1 and 2. Our fit with $b = 1.112$ and consequent difference from the line of equation (5.4) may also be explained by this argument.

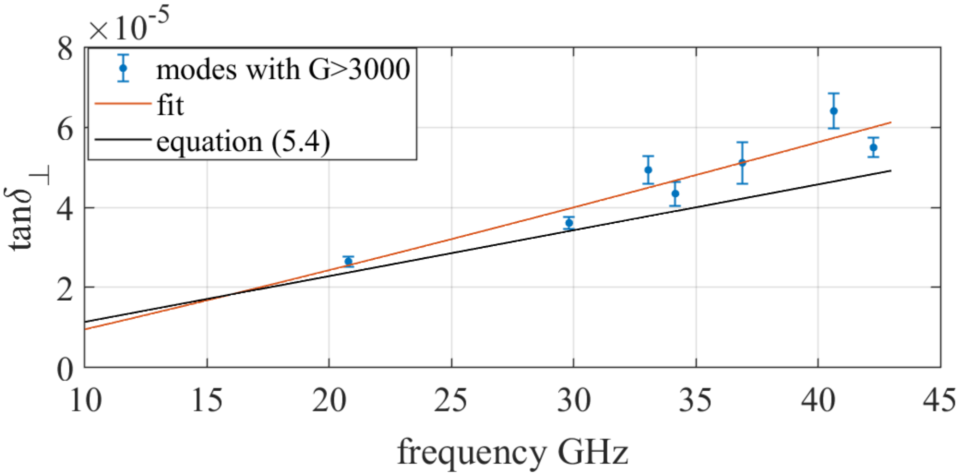

Figure 5.2: $tan\delta_{\perp}$ at room temperature for modes with G bigger than 3000 of both sample 3 and sample 6

Figure 5.3 presents $tan\delta_{\perp}$ of those with G>3000 of sample 3 at 18 K. Since the $P^{||}_{samp}$ of the 32.74, 35.44 and 39 GHz can not be negligible, we should put less credence in these data. We can see that $tan\delta_{\perp}$ first gently goes down and then increases. Consequently, there is a potential minimum around 35 GHz.

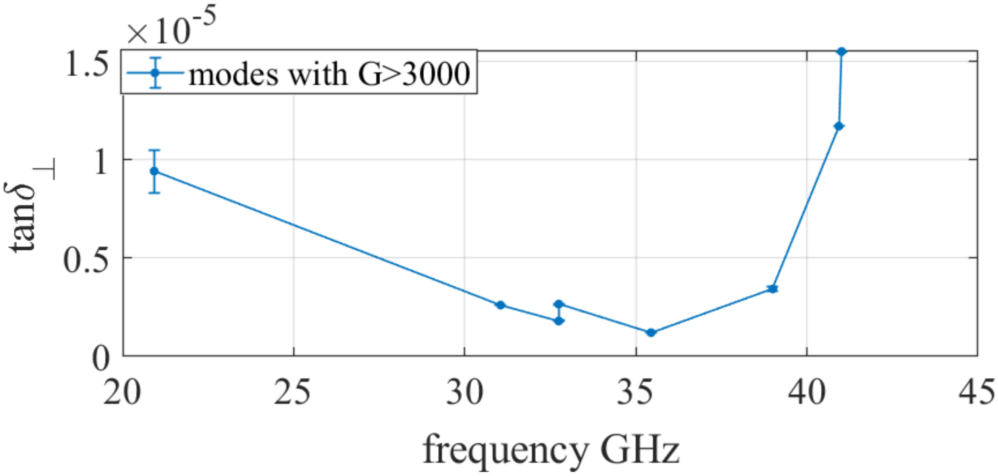

Figure 5.3: $tan\delta_{\perp}$ for sample 3 at 18 K for modes with G larger than 3000

Figure 5.4 shows the loss tangent of 3 different sapphire samples in Braginsky's work. We notice that there is a two-magnitude-order difference in loss tangent at cryogenic temperatures. Above 50 K, these values are close to the model proposed by Gurevich (equation (5.4) and (5.5)). Below 50 K, values of $tan\delta$ are greatly caused by crystal defects. Now look back at our results. The $tan\delta_{\perp}$ we measured at 18 K is 2-magnitude-order larger than that in Breeze's and Krupka's works, one of the reasons can be the imperfections in our samples. Before the minimum in figure 5.3, the loss tangent is mainly caused by defects described by Debye model, which gives a decreasing trend. With the increase in frequency, the loss due to defects is less important and the loss due to the interaction between phonons and electromagnetic waves contributes greatly, which gives the increasing trend. In work by Zuccarro, the decrease in loss tangent caused by defects with the increase in frequency is also observed for $LaAlO_3$ at cryogenic temperatures.

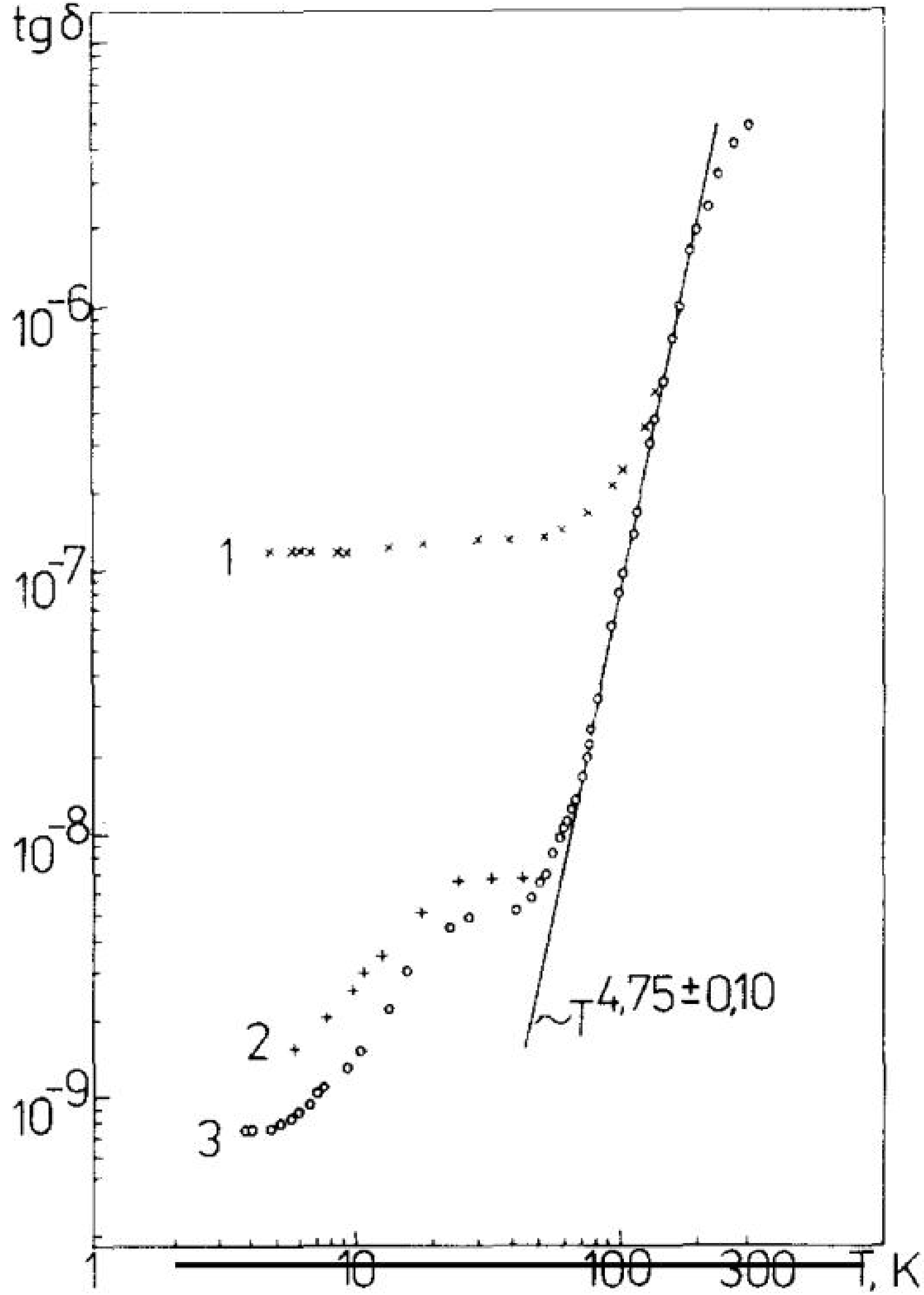

Figure 5.4: Loss tangent of 3 different sapphire samples versus temperature at 9GHz[26]

For $\epsilon_\perp$ at both room temperature and 18 K, we learn that we should use modes with negligible $P^{\|}_{samp}$ and large P_{samp}, so extra plots are made excluding those satisfying these conditions.

Figure 5.5 shows $\epsilon_\perp$ of modes with $P_{samp} > 0.7$ and negligible $P^{\|}_{samp}$ for both sample 3 and sample 6 at room temperature. As we mentioned $\epsilon_\perp$ is almost constant so constant lines are fitted in. The largest relative deviation of sample 3 is 0.12% and for sample 6 it is %0.16.

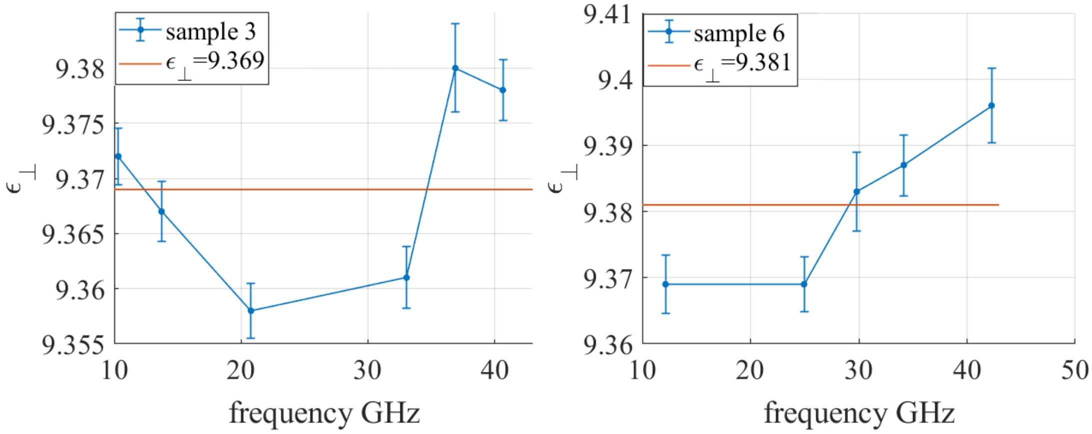

Figure 5.5: $\epsilon_\perp$ for modes with P_{samp}>0.7 and negligible $P^{\|}_{samp}$ of sample 3 (left) and sample 6 (right)

Figure 5.6 shows modes with $P_{samp} > 0.7$ and negligible $P^{\|}_{samp}$ for sample 3 data at 18 K. Again a constant fit is made with $\epsilon_\perp = 9.241$. The largest relative deviation is about %0.14. Note that the $P^{\perp}_{samp}$ of 32.7 and 35.4 GHz modes are not negligible, so we have less confidence in the corresponding data.

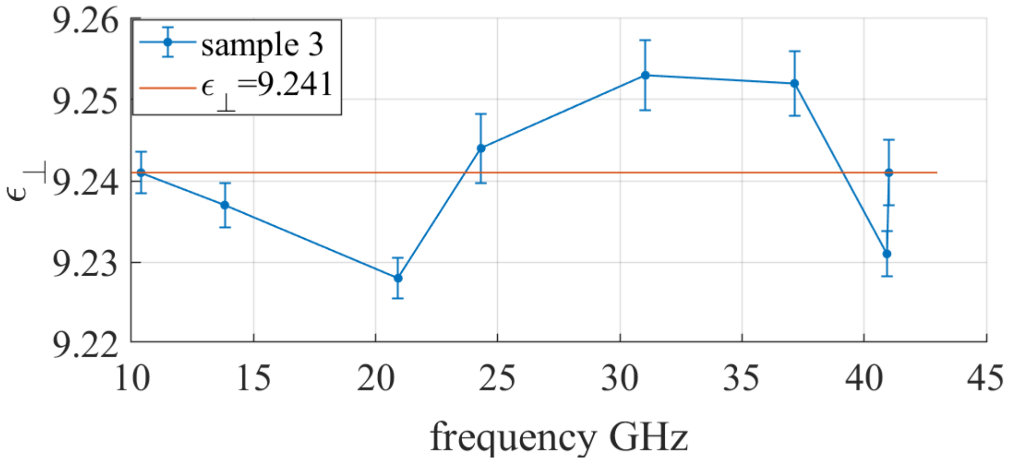

Figure 5.6: $\epsilon_\perp$ for modes of sample 3 with $P^{\perp}_{samp} > 0.7$ and negligible $P^{\|}_{samp}$ at 18 K

The nearly constant behaviour is predicted by equation (5.2). The Debye mode cannot explain our results since it predicts that ϵ decreases with frequency. The relaxation time is given as[27]

$$\tau = \tau_0 e^{\frac{W}{k_B T}} \tag{5.13}$$

where W is the activation energy. We can see that a lower temperature gives a larger relaxation time. Then from equation (5.8), we see the increase in τ leads to the decline in dielectric constant.

Finally, We know from our results and other ones from literature that the measured dielectric properties are sample dependent. The reason is that samples are different in the defect structure, for instance the concentration of impurity ions, the disorientation of crystal growth and dislocations. In the work by Braginsky[26], a block with a disorientation angle about 1°was found in the sample corresponding to curve 1 in figure 5.4. In the work by Belyaev[29], the level of the perfection of sapphire crystals is determined by the growth rate.

6 Summary and Conclusions

We have studied perpendicular components of dielectric constant ($\epsilon_{\perp}$) and loss tangent ($tan\delta_{\perp}$) of sapphire, which is the one of the potential candidate materials for the MADMAX experiment, over the range from 10 GHz to 40 GHz at 295-297 K and at 18 K in a dry cryostat. It is also a relatively rare study over this large frequency range. The fluctuation of $\epsilon_{\perp}$ at both temperatures over the frequency range is less than 1% so $\epsilon_{\perp}$ is almost a constant. At room temperature, $tan\delta_{\perp}$ is almost linearly dependent on frequency which is consistent with Sparks-King-Mill model and explainable by Gurevich model. At 18 K, $\epsilon_{\perp}$ is lower and $tan\delta_{\perp}$ is around 10^{-6} and decided by both phonon electromagnetic wave interaction and defect dipole relaxation processes. In addition, the results seem to be sample dependent. The impurities in samples, the speed of growing crystals and detailed structure of the lattice should be responsible for this. Lastly we see that sapphire meets the requirement to be used in MADMAX dielectric haloscope, indeed with low dielectric loss and high dielectric constant.

A More Mode Identification Results

Figure A.1 and figure A.2 show the results of 1 mm shifted way and PTFE removal way respectively. There are 5 tested modes in each diagram.

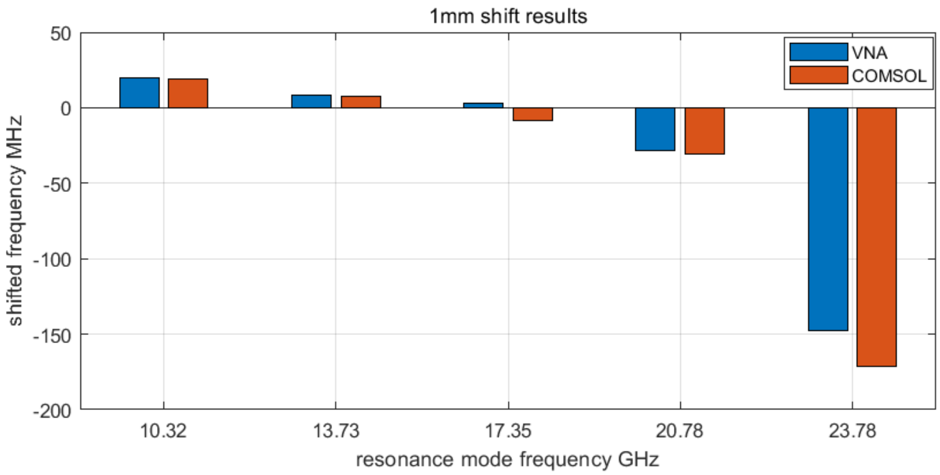

Figure A.1: Comparison of difference in f when the sample is shifted 1 mm away from the center for different modes

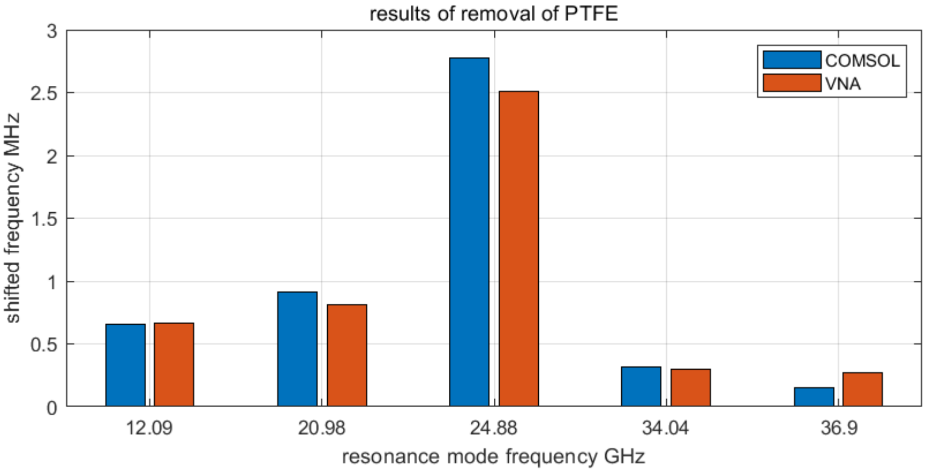

Figure A.2: Comparison of difference in f when the PTFE rod is removed for different modes

Bibliography

[1] R. D. Peccei and Helen R. Quinn. CP conservation in the presence of pseudoparticles. *Phys. Rev. Lett.*, 38:1440–1443, Jun 1977.

[2] Steven Weinberg. A new light boson? *Phys. Rev. Lett.*, 40:223–226, Jan 1978.

[3] Luca Di Luzio, Maurizio Giannotti, Enrico Nardi, and Luca Visinelli. The landscape of qcd axion models. *Physics Reports*, 870:1–117, 2020. The landscape of QCD axion models.

[4] P. Brun, A. Caldwell, L. Chevalier, G. Dvali, P. Freire, E. Garutti, S. Heyminck, S. Knirck, M. Kramer, C. Krieger, T. Lasserre, C. Lee, X. Li, A. Lindner, B. Majorovits, S. Martens, M. Matysek, A. Millar, G. Raffelt, J. Redondo, O. Reimann, A. Ringwald, K. Saikawa, J. Schaffran, A. Schmidt, J. Schütte-Engel, F. Steffen, G. Wieching, C. Strandhagen, and G. Wieching. A new experimental approach to probe QCD axion dark matter in the mass range above 40 μeV. 2019.

[5] Alexander J. Millar, Georg G. Raffelt, Javier Redondo, and Frank D. Steffen. Dielectric haloscopes to search for axion dark matter: theoretical foundations. *Journal of Cosmology and Astroparticle Physics*, 2017(01):061–061, jan 2017.

[6] Stefan Paul Nikolas Knirck. *How To Search for Axion Dark Matter with MADMAX (MAgnetized Disk and Mirror Axion eXperiment).* Dissertation, Technische Universität München, München, 2020.

[7] Kobayashi Yoshio, Fukuoka Nobushige, and Yoshida Shin-Ichiro. Resonant modes for a shielded dielectric rod resonator. *Electronics & Communications in Japan*, 64(11):44–51, 11 1981.

[8] S. Maj and M. Pospieszalski. A composite, multilayered cylindrical dielectric resonator. In *1984 IEEE MTT-S International Microwave Symposium Digest*, pages 190–191, 1984.

[9] J.G. Hartnett, M.E. Tobar, E.N. Ivanov, and J. Krupka. Room temperature measurement of the anisotropic loss tangent of sapphire using the whispering gallery mode technique. *IEEE Transactions on Ultrasonics, Ferroelectrics, and Frequency Control*, 53(1):34–38, 2006.

[10] Jerzy Krupka, Krzysztof Derzakowski, Michael Tobar, John Hartnett, and Richard G Geyer. Complex permittivity of some ultralow loss dielectric crystals at cryogenic temperatures. *Measurement Science and Technology*, 10(5):387–392, jan 1999.

[11] John G. Webster and John Wiley. Wiley encyclopedia of electrical and electronics engineering.

[12] Akihito Ebata, Takashi Shimizu, and Yoshinori Kogami. Frequency dependence measurement of complex permittivity for c-, a- and r-plane sapphire substrates from 30 to 50ghz band. In *2014 Asia-Pacific Microwave Conference*, pages 516–518, 2014.

[13] Jonathan Breeze. *Temperature and Frequency Dependence of Complex Permittivity in Metal Oxide Dielectrics: Theory, Modelling and Measurement*. Springer, 2016.

[14] Patrick Krkotić, Queralt Gallardo, Nikki D. Tagdulang, Montse Pont, and Juan M. O' Callaghan. Algorithm for resonator parameter extraction from symmetrical and asymmetrical transmission responses. *IEEE Transactions on Microwave Theory and Techniques*, 69(8):3917–3926, 2021.

[15] J. Krupka, K. Derzakowski, A. Abramowicz, M.E. Tobar, and R.G. Geyer. Use of whispering-gallery modes for complex permittivity determinations of ultra-low-loss dielectric materials. *IEEE Transactions on Microwave Theory and Techniques*, 47(6):752–759, 1999.

[16] Jerzy Krupka. Measurements of the complex permittivity of low loss polymers at frequency range from 5 ghz to 50 ghz. *IEEE Microwave and Wireless Components Letters*, 26(6):464–466, 2016.

[17] L. G. Hector and H. L. Schultz. The dielectric constant of air at radiofrequencies. *Physics*, 7(4):133–136, 1936.

[18] Frank J. Wentz and Thomas Meissner. Atmospheric absorption model for dry air and water vapor at microwave frequencies below 100ghz derived from spaceborne radiometer observations. *Radio Science*, 51(5):381–391, 2016.

[19] E. Öz. Private communication.

[20] Egorov V.N. and Volovikov A.S. Measuring the dielectric permittivity of sapphire at temperatures 93–343 k. *Radiophysics and Quantum Electronics*, 44, 2001.

[21] Y. Kobayashi and T. Senju. Resonant modes in shielded uniaxial-anisotropic dielectric rod resonators. *IEEE Transactions on Microwave Theory and Techniques*, 41(12):2198–2205, 1993.

[22] Tomasz Karpisz, Bartlomiej Salski, Pawel Kopyt, Jerzy Krupka, and Marcin Wojciechowski. Measurement of uniaxially anisotropic dielectrics with a fabry–perot open resonator in the 20–50 ghz range. *IEEE Microwave and Wireless Components Letters*, 32(5):441–443, 2022.

[23] Simon Ramo, John R Whinnery, and Theodore Van Duzer. *Fields and waves in communication electronics*. John Wiley & Sons, 1994.

[24] N. W. Ashcroft and N. D. Mermin. *Solid State Physics*. Sunders College, 1976.

[25] Norbert Klein. *Microwave Properties and Measurement Techniques*, chapter 5, pages 99–118. John Wiley & Sons, Ltd, 2004.

[26] V.B. Braginsky, V.S. Ilchenko, and Kh.S. Bagdassarov. Experimental observation of fundamental microwave absorption in high-quality dielectric crystals. *Physics Letters A*, 120(6):300–305, 1987.

[27] Claudio Zuccaro, Michael Winter, Norbert Klein, and Knut Urban. Microwave absorption in single crystals of lanthanum aluminate. *Journal of Applied Physics*, 82(11):5695–5704, 1997.

[28] VL Gurevich. Kinetics of phonon systems, 1980.

[29] MV Klassen-Neklyudova, Kh S Bagdasarov, LM Belyaev, et al. Ruby and sapphire, 1974.

[30] M. Sparks, D. F. King, and D. L. Mills. Simple theory of microwave absorption in alkali halides. *Phys. Rev. B*, 26:6987–7003, Dec 1982.

[31] Richard G Geyer et al. Dielectric characterization and reference materials. 1990.